DEM study of the alteration of the stress state in granular media around a bio-inspired probe

Yuyan Chen¹, Alejandro Martinez², and Jason DeJong³

¹Department of Civil and Environmental Engineering, University of California Davis, 2001 Ghausi Hall, Davis, CA 95616; e-mail: yych@ucdavis.edu (*corresponding author)

²Department of Civil and Environmental Engineering, University of California Davis, 2001 Ghausi Hall, Davis, CA 95616; e-mail: amart@ucdavis.edu

³Department of Civil and Environmental Engineering, University of California Davis, 2001 Ghausi Hall, Davis, CA 95616; e-mail: jdejong@ucdavis.edu

ABSTRACT

Soil penetration is a ubiquitous energy-intensive process in geotechnical engineering that is typically accomplished by quasi-static pushing, impact driving, or excavating. In contrast, organisms such as marine and earthworms, razor clams, and plants have developed efficient penetration strategies. Using motion sequences inspired by these organisms, a probe that uses a self-contained anchor to generate the reaction force required to advance its tip to greater depths has been conceptualized. This study explores the interactions between this probe and coarse-grained soil using 3D discrete element modeling. Spatial distributions of soil effective stresses indicate that expansion of the anchor produces arching and rotation of principal effective stresses that facilitate penetration by inducing stress relaxation around the probe's tip and stress increase around the anchor. Spatial strain maps highlight the volumetric deformations around the probe, while measurements of both stresses and strains shows that the state of the soil around the anchor and tip evolves towards the critical state line. During subsequent tip advancement, the stresses and strains are similar to those during initial insertion, leading to the remobilization of the tip resistance. Longer anchor and shorter anchor-to-tip distance better facilitate tip advancement by producing greater stress relaxation ahead of the tip.

Keywords: Discrete element modeling, bio-inspiration, Site investigation, Soil penetration

INTRODUCTION

Soil penetration is a ubiquitous process in geotechnical applications, relevant to activities such as site characterization (Figure 1a), pile driving (Figure 1b), and tunneling, where large equipment (e.g., drill rigs, driving hammers, augers, and cranes) is usually required to provide reaction forces to overcome the penetration resistance. Common accompanying problems in soil penetration processes include inadequate reaction forces (e.g., Mayne 2007), limited access to specific sites (e.g., the toe of a dam, congested urban area, and vegetated areas), and negative environmental impacts (e.g., Raymond et al. 2020; Purdy et al. 2020). These challenges present a need for exploring alternative soil penetration solutions to better achieve engineering functionality and environmental sustainability.

Efficient soil penetration processes may be inspired by organisms that have developed different adaptations for soil penetration and burrowing, such as marine worms (Figure 1c) and growing plant roots (Figure 1d). Many of the adaptations used by these organisms involve concurrent or sequential motions consisting of body expansion/contraction and tip advancement. Polychaetes Alitta virens (Dorgan 2015), Nereis virens (Dorgan et al. 2007; Che and Dorgan 2010), and *Thoracophelia mucronata* (Dorgan 2018) expand their anterior tips to widen cracks laterally and extend cracks anteriorly to achieve forward movement in marine sediments. Tree roots use tip radial growths to weaken soils ahead of tips and enable further tip advancement (Savioli et al. 2014; Ruiz et al. 2015). Earthworms use peristalsis that involves sequential wavelike motions consisting expansion and contraction of their circular muscles; peristalsis allows worms to move within excavated tunnels as well as to loosens the soil ahead of tip (Sadava et al. 2009; Barnett et al. 2009; Kurth and Kier 2014; Ruiz et al. 2015). Razor clams use the 'dual anchor' burrowing strategy, which involves alternating expansion of their foot and shell, to induce stress relaxation ahead of foot and facilitate penetration (Trueman 1968; Murphy and Dorgan 2011; Dorgan 2015). The soil penetration processes used by these organisms resemble the formation of open-mode discontinuities driven by immiscible invasive phases, where

concentration of stresses against the burrow or crack lateral walls induces a relaxation of stresses ahead of burrow or crack tip, as shown in the stress paths in Figure 1e from numerical simulations by Shin and Santamarina (2011).

There has been recent interest in bio-inspired design for geotechnical engineering applications (Martinez et al. 2021). Several investigations focused on the development of new foundations with surfaces that generate direction-dependent friction and soil anchoring elements inspired by tree-roots (e.g., Mallett et al. 2018; Martinez et al. 2019; O'Hara and Martinez 2020; Aleali et al. 2020; Burrall et al. 2020; Stutz et al. 2021). Other experimental and numerical studies on bio-inspired probes and robots also investigated their performance during soil penetration and burrowing. Probes inspired by earthworms, marine worms, and clams use radial body expansion to facilitate soil penetration by reducing the penetration resistance (e.g., Cortes and John 2018; Khosravi et al. 2018; Ma et al. 2020; Ortiz et al. 2019; Huang and Tao 2020; Tao et al. 2020; Huang et al. 2020; Borela et al. 2020; Chen et al. 2020). Plant root-inspired robots also showed high soil penetration efficiency by developing additive tip tissues that reduced the mobilized friction against the robot's embedded surface area (e.g., Sadeghi et al. 2014; Naclerio et al. 2018). Chen et al. (2021) presented the results of 3D discrete element modeling (DEM) simulations of an idealized bio-inspired probe which uses an 'anchor-tip' strategy to penetrate soil. The 'anchor-tip' strategy consists of radially expanding an anchor that mobilizes reaction forces, and subsequently advancing the tip if the mobilized reaction forces are greater than the penetration resistance forces. The study showed that the probe was able to self-penetrate a coarse-grained soil specimen, defined as the ability of a probe to penetrate soil only relying on the reaction force generated by its self-contained anchor.

The studies performed to date have proven that burrowing probes and devices can be functional in different soil types and at different scales. However, less attention has been devoted to the soil failure mechanisms and soil-probe interactions involved in the burrowing processes.

This understanding is required to further optimize probe performance and provide insight of the

geomechanical processes involved in animal and plant burrowing. The DEM study presented herein has the objective of investigating the soil failure mechanisms involved in the expansion of an anchor and subsequent tip advancement of a bio-inspired probe that uses the 'anchor-tip' strategy. The soil failure mechanisms are investigated in terms of spatial distributions of mean, radial, and vertical effective stresses, directions and relative magnitudes of principal stresses, and stress paths at specific locations. DEM simulations of three different probes from Chen et al. (2021) are used to evaluate the effects of probe geometry (e.g., anchor-tip distance H and anchor length L) on the probe responses as well as the state of soil stresses and strains.

MODEL DESCRIPTION

DEM simulations are performed using the PFC 3D software (Itasca, Minneapolis, MN). Each simulation model consists of a bio-inspired probe and a cylindrical virtual calibration chamber (VCC) containing about 210,000 soil particles. The simulated bio-inspired probe is composed of a cylindrical shaft with an initial diameter (D_{probe}) of 0.044 m (cross section area of 15 cm²) and a cone tip with an apex angle of 60° (half apex angle, θ , of 30°), equivalent to the cone penetration testing (CPT) probes routinely used for site characterization (ASTM D 5778-20). The cylindrical shaft consists of multiple radial ring segments that are 0.01 m in height, which allow deploying an anchor with a given length and at a given location behind the tip. The probe friction coefficient (μ_p) is taken as 0.3 for all simulations, which is equivalent to an interface friction angle of 16.7° that is typical of that of conventional CPT friction sleeves (Martinez and Frost 2017; Khosravi et al. 2020).

The cylindrical virtual calibration chamber is 1.2 m in height ($H_{chamber}$), 0.7 m in diameter ($D_{chamber}$), and composed of one top, one bottom, and 14 radial ring walls (Figure 2a). Each wall is individually servo-controlled to achieve constant vertical and radial boundary effective stresses (σ'_z and σ'_r , respectively) throughout the simulations, with $\sigma'_z = 100$ kPa and $\sigma'_r = 50$ kPa, for a $K_0 = \sigma'_r/\sigma'_z = 0.5$. Using 14 radial ring walls to simulate radial boundary

enables a uniform radial stresses of 50 kPa along the VCC's height to be maintained during the penetration and anchor expansion processes (Figure S1 shows the boundary stresses and chamber radii during probe insertion). The constant-stress conditions applied to the chamber boundaries simulate deep penetration conditions (Arroyo et al. 2011; Khosravi et al. 2020). A friction coefficient between particles and wall is 0.1 to improve the stability of servo-control on boundary walls.

The particles are spherical in shape with a mean particle size (D_{50}) of 0.0144 m. The particle size distribution is characterized by a coefficient of uniformity (C_U) and a coefficient of curvature (C_C) of 1.2 and 0.96 respectively. The particle density is taken as 2650 kg/m³, and the specimens are consolidated to an initial void ratio of 0.61. The simulations employ the linear contact model with rolling resistance to simulate the response of sub-rounded to sub-angular soil (Ai et al. 2011; Wensrich and Katterfeld 2012; McDowell et al. 2012), where the sliding and rolling friction coefficients (μ_s and μ_r , respectively) are taken as 0.4 (Table 1). The particle normal stiffness (k_n) is proportional to its diameter (d) with $\frac{k_n}{d} = 10^8 N/m^2$.

As required by most DEM simulations of boundary-value problems, the particle sizes had to be upscaled to maintain reasonable computational costs. The chamber-to-probe diameter $(D_{chamber}/D_{probe})$ and the probe-to-particle diameter (D_{probe}/D_{50}) are 15.9 and 3.1, respectively. These dimensions have been previously shown by Khosravi et al. (2020) and Chen et al. (2021) to reduce potential boundary and particle-scale effects, and are consistent with previous DEM simulations of probe penetration. For example, $D_{chamber}/D_{probe}$ values from 12.0 to 16.6 and D_{probe}/D_{50} values from 2.7 to 3.1 were adopted by Arroyo et al. (2011), Butlanska et al. (2014), Zeng and Chen (2016), Ciantia et al. (2016; 2019), Zhang et al. (2019), and Huang and Tao (2020) in their 3D simulations of probe penetration. Although some other studies employed greater values, such as $D_{chamber}/D_{probe}$ from 30 to 40 and D_{probe}/D_{50} of 21.1, they performed 2D simulations or used symmetric models with only partial chambers simulated (Lin and Wu 2012; Jiang et al. 2006).

The chamber simulated in this study contained 628 measurement spheres (MSs) arranged in the r-z plane (Figure 2b) to obtain the soil stresses and strain rates. Each MS has a diameter of 0.033 m, which leads to an average ratio of the MS volume to particle volume of about 12. The MSs shown in purple in Figure 2b are used to obtain stress paths around the anchor and below the tip.

Model calibration

Kuei et al. (2020) calibrated the contact parameters of the DEM simulations to capture the mechanical response of coarse-grained soils under different overburden stresses. Results of simulations of triaxial compression tests are presented here to examine the element soil responses. Soil specimens were isotropically confined to an initial void ratio (e) of 0.61 under stresses of 5, 25, 100, and 400 kPa, respectively. Then, the soil specimens were compressed in the vertical (i.e. axial) direction while maintaining the radial confining stresses constant. The results show that: (i) shearing the specimens under greater confining pressures led to mobilization of greater peak and residual deviatoric stresses ($q = \sigma_1' - \sigma_3'$) (Figure 3a) and smaller volumetric strains indicating a smaller dilatancy (Figure 3b) and (ii) the stress paths of the tests at different confining stresses converged to a critical state line (CSL) in the q-p' (Figure 3c) and e-p' planes (Figure 3d), where p' is the mean effective stress. The slope of CSL in the qp' plane is 1.46:1, which corresponds to a friction angle of 36.0° and this is consistent with critical state friction angles reported in literature for coarse grained soils (e.g. Simoni and Houlsby 2006; Xiao et al 2016; Yand and Luo 2018). The CSL obtained from the triaxial simulations is used throughout this paper as a reference when plotting the stress paths at select locations within the soil specimen.

To further examine the ability of DEM simulations of modeling the behavior of coarsegrained soils, four CPT simulations using the same model parameters and VCC and probe configurations have been performed at overburden stresses of 5, 25, 100, and 400 kPa. The tip resistance (q_c) values (Figure 3e) increase as the vertical stresses increase and are in agreement with those expected for sub-rounded coarse-grained soils (e.g. Mayne 2007) along with corresponding sleeve friction (f_s) values (Chen et al. 2021). When plotting the CPT results on the soil behavior type chart by Robertson (2016) using the normalized tip resistance and sleeve friction, the data points indicate a classification between 'sand-like contractive' and 'sand-like dilative' (Figure 3f). The results of CPT simulations provide confidence in the ability of the DEM model to reproduce a penetration response that is representative of coarse-grained soils.

Bio-inspired probe and simulation sequence

The simulated bio-inspired probe consists of an anchor that can expand radially and a tip that is advanced vertically down (Figure 4a). The two important probe configuration parameters discussed in this paper are the anchor length (L) and the anchor-tip distance (H). The simulations include three stages (Figure 4b) which use a simplified sequence of motions to approximate those of a physical probe. First, during the cone penetration (CP) stage the probe is inserted into soil at a constant rate of 0.2 m/s to a target depth of 0.9 m while the q_c (Eq. 1) and f_s (Eq. 2) are recorded. This motion is similar to that employed during CPT testing (ASTM D5778-20). During the anchor expansion (AE) stage, the probe is stopped and the diameter of the anchor is uniformly expanded at a rate of 0.2% per second of its initial diameter (D_{probe} = 0.44 mm) until a target diameter (D_{anchor}) of 0.066 mm is achieved while the radial anchor pressure (P_a) and end bearing anchor pressure (P_b) are measured. This motion is similar to that employed during inflation of a pressuremeter probe in the field (Mair and Wood 1987).

$$q_{c} = \frac{4\sum_{i=1}^{N} Q_{Ztip,i}}{\pi D_{probe}^{2}}$$

$$f_{s} = \frac{\sum_{i=1}^{N} Q_{zsleeve,i}}{0.16\pi D_{probe}}$$

$$(1)$$

During the tip advancement (TA) stage, the anchor is displaced upward while the tip is displaced downward using a velocity-controlled algorithm with force limits (Figure 5). This algorithm is analogous to the force loading control mechanisms used in standard laboratory

testing, such as cyclic triaxial and cyclic simple shear testing, which applies a constant velocity until a target force is generated. It is noted that this type of control algorithm does not require for the reaction and resistance forces to be in equilibrium. In the DEM simulations, the motions of a probe section (i.e. the anchor or the tip) are updated at each timestep by comparing the forces acting on them (i.e. total reaction or resistance force, F_t or Q_t , respectively) against the target force (F_{target}). When a probe section mobilizes a force that is smaller than F_{target} , it will be displaced at a velocity of 0.2 m/s (downward for the tip and upward for the anchor). The initial value of F_{target} is zero, and it is increased by a small constant increment of 50 N subsequently (i.e. $F_{target,1} = 50 \text{ N}$, $F_{target,2} = 100 \text{ N}$, etc.). The F_{target} increment was chosen based on iterative calibration that showed that a increments smaller than or equal 50 N have no influence on the results. The tip advancement simulation is terminated when the upward anchor displacement is greater than 0.04 m (about 1 D_{probe}), indicating failure to mobilize enough anchorage, or when the downward tip displacement is greater than 0.14 m, which is considered as successful tip advancement.

The forces acting on the probe during the TA stage are the total reaction force (F_t), defined as the sum of anchor friction force (F_a , Eq. 3) and end bearing force (F_b , Eq. 4), and the total resistance force (Q_t), defined as the sum of the tip resistance force (Q_c , Eq. 5) and the shaft resistance force (Q_s , Eq. 6). Using the control algorithm with force limits, the anchor and tip are controlled separately, as previously described (i.e. Fig. 5).

$$F_a = 2\pi P_a L D_{anchor} \mu_p \tag{3}$$

$$F_b = \frac{\pi}{4} P_b \left(D_{anchor}^2 - D_{probe}^2 \right) \tag{4}$$

$$Q_c = \frac{\pi}{4} q_c D_{probe}^2 \tag{5}$$

$$Q_{s} = \pi f_{st} D_{probe} \tag{6}$$

Where $Q_{ztip, i}$ is the vertical component of the contact force i acting on the probe tip, $Q_{zsleeve, i}$ is the vertical component of the contact force i acting on the bottom 0.16 m of probe shaft, f_{st} is

the average shear stress along the entire probe shaft, and N is the total number of vertical contact forces acting on the tip or sleeve.

Five simulations are performed in this study to examine the influence of the probe configuration on the probe-soil interactions (Table 2). Simulation #1 is used as the reference case throughout this paper, which is for the probe with the anchor-tip distance $H = 4D_{probe}$ and the anchor length L = 4 D_{probe} . Simulations #2 and #3 use the same soil specimen as the reference simulation but have different probe configurations. For the ease of comparison, Simulations #1, #2 and #3 are given names with the format HXLY to reflect the probe configuration, where X represents the value of H in D_{probe} equivalents and Y represents the value of L in D_{probe} equivalents. For example, simulation "H1L4" represents the simulation for the probe with anchor-tip distance $H = 1D_{probe}$ and anchor length L = 4 D_{probe} . Two additional simulations (#4 and #5) were performed with probes on independently generated specimens with the H4L4 configuration. These simulations were performed to assess the variability in the simulation resulting from using different specimens; these simulations are identified with the suffixes 'R1' and 'R2'.

According to contact dynamics, the inertial number (I), which quantifies the inertial forces on grains relative to the skeleton forces, should be smaller than 10^{-3} to maintain quasi-static conditions (Combe and Roux 2019; Radjai and Richefeu 2009; O'Sullivan 2011). The inertial numbers during the three stages in this study were calculated as follows: between 2.1×10^{-5} and 4.4×10^{-4} during CP, between 2.1×10^{-5} and 3.6×10^{-4} during AE, between 1.1×10^{-6} a 7.2×10^{-4} during TA. The overlap between particles and between particles and walls was also measured throughout the simulations. During all three stages, the overlap of 99% of the simulated particles remained smaller than 1% of the particle radius.

GLOBAL-SCALE RESULTS

The results of the simulations from a global perspective are first described, where the evolution of forces and pressures acting on the probe during the entire three simulation stages are summarized to show their evolution during the different simulation stages. Then, the proceeding three sections examine in detail the meso-scale results (i.e. states of stress and strain) during the CP, AE, and TA simulation stages to characterize the soil failure mechanisms and provide further insight into the evolution of the resistance and reaction forces acting against the probe.

The CP stage has a significantly greater time duration than the AE and TA stages due the target penetration depth of 0.9 m. For visualization purposes, the results in this section are presented in terms of a normalized timestep (\overline{N}) to highlight the evolution history of probe measurements and displacements throughout the entire simulations. \overline{N} is defined by Eq. 7 such that values from 0 to 1 represent the CP stage, 1 to 2 represent the AE stage, and 2 to 3 represent the TA stage:

$$\overline{N} = \begin{cases} n/n_1 & (n \le n_1) \\ 1 + (n - n_1)/(n_2 - n_1) & (n_1 < n \le n_2) \\ 2 + (n - n_2)/(n_3 - n_2) & (n > n_2) \end{cases}$$
(7)

where n is the time step and n_1 , n_2 , and n_3 are the time steps at the end of CP, AE, and TA stages, respectively. Note that \overline{N} is not the computational timestep in DEM, which differs among different simulation stages and is determined by the minimum eigen-period of the total system and of the particle mass and contact stiffness matrix (Cundall and Strack 1979; Potyondy 2009).

Cone Penetration (CP), Anchor Expansion (AE), and Tip Advancement (TA)

Figures 6a, 6d, and 6e show the probe pressures and displacements for the three simulations with different anchor configurations. As the probe is inserted into the VCC during CP (i.e. increase in tip vertical displacement) ($\overline{N} \in [0,1]$) the penetration resistance (q_c) increases to an average value of 4.8 MPa (with variations between 3 and 6 MPa, Figure 6). During this stage, the measurements are the same for all three simulated probes because their tips are identical. During AE (i.e. increase in anchor radial expansion) ($\overline{N} \in [1,2]$), the anchor radial pressure (P_a) and end bearing pressure

 (P_b) increase as the anchor is radially expanded. The value of P_a approaches an asymptotic limiting pressure (P_L) at the end of AE $(\overline{N}=2)$, which is observed to be independent of the anchor-tip distance (H) but decreases as the anchor length (L) is increased. For example, a P_L value of 753 kPa is developed during simulation H4L4 (Figure 6a) and 780 kPa in simulation H1L4 (Figure 6b), whereas the P_L value for simulation H4L8 is around 550 kPa (Figure 6c). The P_L values in this study are consistent with previous simulations using cavity expansion that predict P_L values between 600 and 1000 kPa for mildly dilatant sands with friction angles between 30 and 36° (Yu and Houlsby 1991; Salgado and Prezzi 2007; Martinez et al. 2020). Expansion of the anchor results in a decrease of q_c . Greater decreases in q_c are observed for the simulations with smaller H and greater L. For instance, in simulation H4L4 the q_c decreased from a value of 4.8 MPa at the end of CP ($\overline{N}=1$) to a value of 3.4 MPa at the end of AE ($\overline{N}=2$) (Figure 6a), while q_c decreased from a value of 4.8 MPa at the end of CP to values of 2.0 MPa and 3.2 MPa during simulations H1L4 (Figure 6b) and H4L8 (Figure 6c), respectively. The reduction in q_c is in agreement with the 3D DEM results presented by Huang and Tao (2020), who reported a reductions between 10% and 40% during expansion of a cylindrical anchor located immediately behind the tip of a bio-inspired probe.

During TA ($\overline{N} \in [2,3]$) the anchor is displaced upward (i.e. decrease in vertical displacement) and the tip is displaced downward (i.e. increase in vertical displacement) using velocity-controlled motion with force limits. At the early stages of TA (e.g., at $\overline{N} < 2.55$, 2.3, and 2.7 which are marked with red arrows in Figures 6a-6c and 7a–7c, respectively), the anchor remained stationary while the tip was displaced downward because the total reaction force (F_t) was greater than the total resistance force (F_t). During this period, there is slight decrease in both anchor radial pressure (F_t) and end bearing pressure (F_t), which is due to the tip penetration. As the TA stage continued, the anchor was displaced upward because the target force (F_t) exceeded F_t . This upward displacement of the anchor led to a decrease in F_t and an increase in F_t . At the end of TA (F_t), F_t 0 are reached a slightly smaller value than the F_t 1 are and F_t 2. The end of CP (F_t 3 are reached a slightly smaller value than the F_t 3 and F_t 4.

MPa for simulations H4L4, H1L4, and H4L8, respectively, compared to a q_c value of 4.8 MPa at the end of CP. The DEM simulation results from Huang and Tao (2020) also show a remobilization of q_c to values that are slightly smaller than those measured before anchor expansion. During the TA stage of simulations H4L4, H1L4, and H4L8, the tip penetrated to depths of 0.936 m, 1.05 m, and 1.04 m, respectively, indicating that both a shorter anchor-tip distance (H) and a longer anchor length (L) enable greater tip penetration displacements.

To assess the possible effects of using the same specimen for all the simulations, two additional reference simulations were performed on independently-generated specimens with the reference probe (i.e. H4L4). A summary of the pressures generated at the end of the three simulation stages are provided in Table 3. The results indicate a small variabilities in q_c during the CP, AE, and TA stages (coefficients of variation (COV) of 0.6%, 6.8%, and 3.9%, respectively). The P_a values during the AE and TA stages also showed relatively small variabilities (COV of 4.9% and 7.5%), while the P_b values during the TA stage show a somewhat greater variability (COV of 17.6%). Nonetheless, the three simulations show similar trends, with a decrease in q_c and an increase in P_a during the AE stage and an increase in q_c , decrease in P_a , and increase in P_b during the TA stage, indicating that the conclusions drawn from the simulations are independent on the inherent variability in the simulations.

MESO-SCALE RESULTS

State of stresses and strains during Cone Penetration (CP)

The state of stresses at the end of CP can be visualized by means of force chain maps, which highlight contact forces within the simulated granular assembly, as shown in Figure 8a where the normal contact forces between the particles and between the particles and the probe greater than 50 N are represented by lines whose thickness and color represent the contact force magnitude. As expected, Figure 8a indicates that force chains with greater magnitudes occur near the probe tip which generate the penetration resistance. While DEM only solves discrete quantities (e.g.,

contact force, particle displacement), continuum quantities such as stress and strain can be obtained by applying averaging algorithms over an area or volume of interest (e.g., Christoffersen et al. 1981; Fortin et al. 2003). The relative difference between the major (σ'_1) and minor (σ'_3) principal stresses as well as their orientation is visualized in Figure 8b using crosses, where the longer line represents the orientation and relative magnitude of the major principal stress and the shorter line represents the orientation and magnitude of the minor principal stress. Due to the K_0 conditions applied to the specimens, σ'_1 was initially aligned in the vertical direction. As shown, there is significant rotation of principal stresses near the probe tip. Namely, the direction of σ'_1 progresses from horizontally aligned near the cone shoulder to vertically aligned below the cone tip. These results are in agreement with those presented in other studies of CPT and pile penetration (i.e., Jiang et al. 2006; Ciantia et al. 2019). The major principal stresses around the probe shaft are oriented in average at 30° to 70° from horizontal. The intermediate principal stresses (σ'_2) are not considered in this 2D cross plot, but they are considered in the stress paths presented in the proceeding sections.

During CP, the soil near the probe tip is subjected to large magnitudes of mean, radial, and vertical effective stresses, as shown in Figures 9a–9c. The figures show stress maps at the end of the CP stage ($\overline{N} = 1$), where each square represents the average stress in a measurement sphere at that specific location. The effective stresses are concentrated in an area around the tip with a radius of 2 to 4 times the probe diameter, in agreement with previous DEM simulations of CPT or pile insertion processes (e.g., Ciantia et al. 2019; Zhang et al. 2015).

Figures 9d–9f show the volumetric, radial, and vertical strain maps for the last 0.1 m of penetration during the CP stage, where dilative volumetric strains and compressive strain components are defined as positive. As the tip is displaced downward, soil dilatancy ahead of the tip is observed in the ε_v map (Figure 9d); the soil radially around the tip experiences compressive ε_r while the soil below the tip experiences tensile ε_r (Figure 9e). In contrast, the soil radially

around the tip experiences tensile ε_z while the soil below the tip experiences compressive ε_z (Figure 9f).

Stress paths represent the evolution of the three-dimensional stress state. This analysis presents stress paths obtained from locations around the anchor and ahead of the tip (e.g., purple measurement spheres in Figure 2b) for the last 0.1 m of probe penetration. Figures 10a and 10b show the stress paths in the q-p' and e-p' planes. The critical state lines (CSLs) obtained from triaxial compression simulations (Figures 3c and 3d) are included here and used as a reference. In addition, Figure 10c shows the influence of the intermediate stress by means of the b value, where b is defined as:

$$b = (\sigma'_2 - \sigma'_3)/(\sigma'_1 - \sigma'_3).$$

where b = 0 indicates the stress state during conventional triaxial testing (i.e. $\sigma'_2 = \sigma'_3$).

The stress paths are the same for the three different simulations (Figures 10a–10c) because the CP stage is identical for all simulations. As the probe is advanced into the specimen, the particles ahead of the tip are loaded in compression and the stress paths plot slightly above the triaxial CSL, consistent with previous experimental and numerical investigations on cone penetration and pile installation processes (e.g., Jardine et al. 2013; Jiang et al. 2006; Sheng et al. 2005). This is likely because the soil ahead of tip has not exhausted its dilatancy potential and has not reached critical state, as shown by the stress paths in the e-p' plane that have not reached the CSL (Figure 10b). The stress path near the tip is closer to reaching the CSL in the q-p' plane than in the e-p' plane. While critical state conditions would be expected near the probe tip, it should be considered that the measurement spheres are located 0.1 m below the tip to allow for the subsequent downward movement of the tip during the TA. The b-values have magnitudes between 0.05 and 0.15, indicating similar magnitudes of σ'_2 and σ'_3 which closely resemble the stress conditions during conventional triaxial testing.

The stress paths at locations near the anchor indicate that the soil is unloaded as the probe moves downward (Figure 10a). The stress path of the soil around the H1L4 anchor shows the

greatest decrease in p', while the stress path for the soil around the H4L8 anchor shows the smallest decrease in p', as observed in the Figures 10d and 10e. In addition, Figure 10e shows that the void ratio around the three anchors remains fairly constant during the last 0.1 m of the CP stage because the deformations in these locations are small. The *b-values* near the anchor have magnitudes between 0.33 and 0.18, indicating a greater influence of the intermediate stress.

State of stresses and strains during Anchor Expansion (AE)

For all three simulated probes, AE led to an increase in interparticle and particle-probe contact forces at locations around the anchors. Simultaneously, AE led to a decrease in contact forces at locations between the anchors and tips and near the probe tips, as shown by the force chain maps at the end of AE ($\overline{N} = 2$) (Figures 11a–11c). The cross plots indicate that σ'_1 is oriented horizontally around the probes (Figures 11d–11f), perpendicular to the surface of the expanded anchors. This constitutes a rotation 90° of the principal stresses with respect to that at the end of anisotropic consolidation with $K_0 = 0.5$ and a rotation of 60° to 20° with respect to the end of the CP stage. The σ'_1 near the tip decreased in magnitude (i.e., shorter cross length) with respect to the end of CP (i.e., Figure 8b), but the orientation of the principal stresses remains relatively unchanged. There is an absence of force chains with a magnitude greater than 50 N between the anchor and the tip, particularly for simulations H4L4 and H4L8, showing the reduction in contact forces at those locations due to arching.

The stress maps for the three simulations indicate that the normal stresses around the anchor increased while the stresses at locations ahead of the anchor decreased, particularly close to the tip. This is shown in Figures 12a–12i in terms of the difference in normal stresses between the end of the AE ($\overline{N} = 2$) and CP ($\overline{N} = 1$) stages. The increase in mean, radial, and vertical stresses around the anchors is accompanied by soil dilatancy (i.e., positive ε_v) owing to the initially dense state of the specimen, as well as radial compressive stains ε_r (Figures 13a–13f).

At locations near the probe tip, the mean, radial, and vertical decreased as a result of the anchor expansion (Figures 12a–12i), which are accompanied by vertical tensile strains (Figures 13g–13i). It is noted that a greater decrease in stresses occurs during simulations with shorter anchor-tip distance (Simulation H1L4 in Figures 12b, 12e, and 12h). In addition, the longer anchor in Simulation H4L8 deforms a greater volume of soil compared to the shorter anchors (Figures 13a-13i). Altogether, these comparisons highlight the effects of the probe configuration on the alteration of stress states and soil deformations.

The increase in stresses around the expanded anchor are in agreement with the DEM results by Ma et al. (2020) and Huang and Tao (2020). In addition, the reduction in stresses at locations near the tip have also been reported by Huang and Tao (2020). The deformations around the cylindrical anchor are in agreement with the shear deformations at the initial stages of inflation around an expanding conforming balloon reported by Ma et al. (2020) (referred to by the authors as the balloon). However, at the latter stages of inflation, the balloon in the Ma et al. (2020) study took a near-circular cross-section which led to compaction and increases in stresses at locations immediately above and below the balloon. In contrast, the state of stresses and deformations of the soil at the ends of the cylindrical anchor modeled in these simulations, as well as that simulated by Huang and Tao (2020), appears to be highly influenced by arching which causes the reported decrease in stresses. This comparison sheds some light on the effects of the anchor shape (i.e. cylindrical versus spherical) on the changes in state of stress and the associated mobilized anchorage forces.

The expansion of the anchor results in a decrease of the soil stresses below the probe the tip, as previously described. These changes in stress produce stress paths that unload along the CSL in the three simulations (Figure 14a). Because the volume changes at these locations are small (Figure 13a–13c), the void ratio only increases slightly while p' decreases (Figure 14b). The *b*-values at locations below the tip increase slightly as the anchor is expanded, likely due to the greatest decrease in vertical effective stresses (Figures 12a–12i).

The stresses at locations around the anchor increase significantly, as shown by the stress paths that move up and to the right towards the CSL in the q-p' plane (Figure 14d). The increase in p' is smallest for the H4L8 simulation owing to the greater length of the anchor, as previously described. The increase in p' is greater for the H1L4 simulation than for the H4L4 simulation. In the e-p' plane, the stress paths appear to converge towards the CSL, showing initial contraction (i.e. decrease in e) followed by continued dilation (i.e. increase in e) (Figure 14e). This increase in void ratio is in agreement with increases in porosity of up to 20% around the balloon anchor reported by Ma et al. (2020). The b-values increase sharply at the initial stages of AE indicating a divergence of the magnitudes of the minor and intermediate principal stresses. At the end of the anchor expansion phase ($\overline{N} = 2$), and b-values converge to values between 0.2 and 0.3.

State of stresses and strains during Tip Advancement (TA)

This section describes the evolution of the state of stresses and strains during the TA simulation stage. During TA, the tip is displaced downward and the anchor is displaced upward using velocity-controlled motion, such that the tip is displaced downward when Q_t is smaller than F_{target} and the anchor is displaced upward when F_t is smaller than F_{target} (i.e., Figure 5). Figures 15a–15c present the force chain maps at the end of the TA stage ($\overline{N} = 3$). As shown, force chains with greater magnitude are concentrated near the tip and around the anchor. Stronger force chains around the probe tip occur at the end of TA than at the end of AE (i.e., Figures 11a–11c), indicating that as the tip was displaced downward the tip resistance was remobilized. Some force chains are oriented horizontally around the expanded anchor. However, strong force chains are also present at the upper base of the anchors, reflecting the mobilization of the P_b resistance as the anchor is displaced upward (i.e., Figures 6a, 6d and 6e). The cross plots shown in Figures 15d–15f indicate similar trends at locations near the tip and around the anchor as described for the CP and AE stages. The most significant rotation of principal stresses can be observed at the

top base of the anchor, with the major principal stress are oriented at angles between 30 and 50° from horizontal.

The stress maps for the mean, radial, and vertical stresses, expressed in terms of the difference in stress at the end of the TA and AE stages, indicate an increase in stresses at locations below the tip and above the anchor, and decreases in stresses at locations around the anchor and behind the tip (Figures 16a–16i). A greater increase in stresses near the tip occurs for probes with shorter H (Figures 16b, 16e, and 16h) and longer anchor length L (Figures 16c, 16f, and 16i) because during these simulations the tip was displaced by a greater distance, as shown in Figures 7b–7c. The probe with shorter H achieves this by decreasing q_c to a smaller magnitude after AE, whereas the probe with longer L mobilizes a greater reaction force due to its greater contact area with the surrounding particles.

The strain maps presented in Figures 17a–17i show similar trends near the probe tip as those observed at the end of the CP stage (i.e., Figures 9d–9f), with positive (dilative) volumetric and vertical (compressive) strains and negative (tensile) radial strains below the tip and positive (compressive) radial strains and negative (tensile) vertical strains around the probe shoulder. The strains around the anchor show small contractive volumetric strains which possibly lead to the decrease in anchor friction force. Additionally, greater strains are shown behind the anchor base due to the anchor's upward movement.

The stress paths during the TA phase at locations below the tip for the first 0.036 m of downward tip displacement are presented, showing similar trends as described for the CP stage. Namely, p' increases and the stress paths follow the CSL in the q-p' plane (Figure 18a). In the e-p' plane, the stress paths show slight dilation accompanied with increase in p' (Figure 18b). As previously described for the CP stage, the b-values are between 0.1 and 0.15 (Figure 18c). The stress paths at locations around the anchor indicate a decrease in p' while the stress paths follow the CSL (Figure 18d) with minimal changes in void ratio (Figure 18e). The p' around the anchor in simulation H4L4 decreased by a greater amount because at this stage of the simulation (0.036

m of tip displacement), the anchor had displaced 0.04 m upward (Figure 7a), whereas the anchors in the H1L4 and H4L8 simulations had displaced a smaller amount (Figures 7b and 7c). The *b-values* around the anchor stay relatively constant at values between 0.2 and 0.3 (Figure 18f), indicating a greater influence of the intermediate major stress as compared to locations below the tip.

CONCLUSIONS AND FUTURE NEEDS

This study presents a 3D discrete element modeling analysis of the alteration of the state of soil stresses around a probe that employs a the 'anchor-tip' burrowing strategy. The penetration simulations are performed in a virtual calibration chamber that applies constant stress boundary conditions to an medium-dense assembly to model deep penetration simulations. The DEM simulation parameters are calibrated to reproduce realistic coarse-grained soil behavior (i.e. stress-dependent shear strength and dilatancy, convergence to critical state, penetration resistances typical of sands and gravels). Simulations are performed on three different bio-inspired probes to explore the effects of the anchor-tip distance and the anchor length.

During the initial stage the bio-inspired probe penetration simulations, termed Cone Penetration, the probe is advanced into the specimen confined in the VCC in a similar manner as a CPT sounding. The results are in agreement with published trends, with contact forces concentrating near the probe tip which lead to increases in mean, radial, and vertical effective stresses, rotation of principal effective stresses to directions that are close to perpendicular to the surface of the probe's conical tip, and a gradual convergence towards the critical state line in the stress and compression planes of the soil located below the probe tip.

The second stage consists of radially expanding the cylindrical anchor from its initial diameter to a diameter 50% greater. As the anchor is expanded, large contact forces are generated radially around the anchor leading to large increases in mean, radial, and vertical effective stresses and a rotation of 90° the major principal effective stresses. Significant arching

is developed at locations above and below the anchor, leading to tensile strains and a decrease in effective stresses at locations near the probe tip. The soil at locations near the probe continues to converge towards the CSL, with the soil around the anchor dilating due to its initially dense state.

In the Tip Advancement stage, a dynamic control algorithm is used to displace the tip and anchor such that only the probe portion (i.e. tip or anchor) that mobilizes a force smaller than the target force is displaced. Strong contact forces develop at the upper base of the anchor due to the mobilization of a bearing anchor pressure which results in increases in stresses and rotation of principal stresses. The stresses within the soil around the anchor decrease due to contractive volumetric strains, leading to the reduction in the anchorage friction force. The soil response around the tip is similar to that during Cone Penetration, leading to the remobilization of the tip resistance.

The results and analysis of this study expand on the current understanding of the soil failure mechanisms involved in the penetration behavior of bio-inspired probes with radially expanding sections which considers the effects of the probe configuration. The use of the control algorithm with force limits revealed that that longer anchors and smaller anchor-tip distances are more advantageous for the tip advancement process because they lead to greater arching-induced reductions in tip resistance and to mobilization of greater anchorage forces. In the future, a number of advances should be implemented to further understand the behavior of this type of bio-inspired probes and to ultimately lead to their successful deployment in the field: (i) include in the simulation the processes of anchor retraction along with expansion of a second anchoring section near the probe tip in order to model entire self-burrowing cycles, (ii) validate the simulation results with experimental results to assess the possible effects of the upscaled particle sizes and the stress-controlled VCC employed in this study, (iii) investigate the effects of soil parameters such as void ratio, friction angle, and particle size distribution, and (iv) simulate other more complex bio-inspired burrowing strategies in conjunction with anchor expansion, such as tip vibration.

ACKNOWLEDGEMENTS

This material is based upon work supported in part by the Engineering Research Center Program of the National Science Foundation under NSF Cooperative Agreement No. EEC-1449501). The first and second authors were supported by the National Science Foundation (NSF) under Award No. 1942369. Any opinions, findings, and conclusions or recommendations expressed in this material are those of the author(s) and do not necessarily reflect those of the National Science Foundation.

REFERENCES

- Ai, J., Chen, J.F., Rotter, J.M., and Ooi, J.Y. 2011. Assessment of rolling resistance models in discrete element simulations. Powder Technology, 206(3): 269–282. doi:10.1016/j.powtec.2010.09.030.
- Aleali, S.A., Bandini, P., and Newtson, C. M. 2020. Multifaceted bioinspiration for improving the shaft resistance of deep foundations. Journal of Bionic Engineering, **17**(5): 1059–1074. doi:10.1007/s42235-020-0076-6.
- Arroyo, M., Butlanska, J., Gens, A., Calvetti, F., and Jamiolkowski, M. 2011. Cone penetration tests in a virtual calibration chamber. Géotechnique, **61**(6): 525–531. doi:10.1680/geot.9.P.067.
- ASTM D5778-20. Standard test method for electric friction cone and piezocone penetration testing in soils. ASTM International.
- Barnett, C.M., Bengough, A.G., and McKenzie, B.M. 2009. Quantitative image analysis of earthworm-mediated soil displacement. Biology and fertility of soils, **45**(8): 821–828. doi: 10.1007/s00374-009-0392-9.
- Borela, R., Frost, J.D., Viggiani, G., and Anselmucci, F. 2020. Earthworm-inspired robotic locomotion in sand: an experimental study using x-ray tomography. Géotechnique Letters, 1–22. doi:10.1680/jgele.20.00085.
- Burrall, M., DeJong, J.T., Martinez, A., and Wilson, D.W. 2020. Vertical pullout tests of orchard trees for bio-inspired engineering of anchorage and foundation systems. Bioinspiration and Biomimetics, **16**(1). doi:10.1088/1748-3190/abb414.
- Butlanska, J., Arroyo, M., Gens, A., and O'Sullivan, C. 2014. Multi-scale analysis of cone penetration test (CPT) in a virtual calibration chamber. Canadian Geotechnical Journal, **51**(1): 51–66. doi:10.1139/cgj-2012-0476.

- Che, J. and Dorgan, K.M. 2010. It's tough to be small: dependence of burrowing kinematics on body size. Journal of Experimental Biology, **213**(8): 1241–1250. doi:10.1242/jeb.038661.
- Chen, Y., Khosravi, A., Martinez, A., and DeJong, J. 2021. Modeling the Self-Penetration Process of a Bio-Inspired Probe in Granular Soils. Bioinspiration and Biomimetics, **16**(4) 046012 doi:10.1088/1748-3190/abf46e.
- Chen, Y., Khosravi, A., Martinez, A., DeJong, J., and Wilson, D. 2020. Analysis of the Self-Penetration Process of a Bio-Inspired In Situ Testing Probe. Geo-Congress 2020: 224–232.
 Reston, VA: American Society of Civil Engineers. doi:10.1061/9780784482834.025
- Christoffersen, J., Mehrabadi, M.M., and Nemat-Nasser, S. 1981. A micromechanical description of granular material behavior. Journal of Applied Mechanics, **48**(2): 339–344. doi:10.1115/1.3157619.
- Ciantia, M.O., Arroyo, M., Butlanska, J., and Gens, A. 2016. DEM modelling of cone penetration tests in a double-porosity crushable granular material. Computers and Geotechnics, 73: 109–127. doi:10.1016/j.compgeo.2015.12.001
- Ciantia, M., O'Sullivan, C., and Jardine, R.J. 2019, September. Pile penetration in crushable soils: Insights from micromechanical modelling. In 17th European Conference on soil Mechanics and Geotechnical Engineering (ECSMGE 2019). International Society for Soil Mechanics and Geotechnical Engineering. doi:10.32075/17ECSMGE-2019-1111.
- Combe, G. and Roux, J.N. 2009. Discrete numerical simulation, quasistatic deformation and the origins of strain in granular materials. arXiv:0901.3842.
- Cortes, D. and John, S. 2018, September. Earthworm-inspired soil penetration. In Proceedings of the 1st Biomediated and Bioinspired Geotechnics (B2G) Conference. Atlanta.
- Collins, I.F., Pender, M.J., and Yan, W. 1992. Cavity expansion in sands under drained loading conditions. International Journal for Numerical and Analytical Methods in Geomechanics, 16(1):3–23. doi:10.1002/nag.1610160103.

- Cundall, P.A. and Strack, O.D. 1979. A discrete numerical model for granular assemblies. Geotechnique, **29**(1): 47–65.
- Dorgan, K.M. 2015. The biomechanics of burrowing and boring. Journal of Experimental Biology, **218**(2): 176–183. doi:10.1242/jeb.086983.
- Dorgan, K.M. 2018. Kinematics of burrowing by peristalsis in granular sands. Journal of Experimental Biology, **221**(10). doi:10.1242/jeb.167759.
- Dorgan, K.M., Arwade, S.R., and Jumars, P.A. 2007. Burrowing in marine muds by crack propagation: kinematics and forces. Journal of Experimental Biology, **210**(23): 4198–4212. doi:10.1242/jeb.010371.
- Fortin, J., Millet, O., and de Saxcé, G. 2003. Construction of an averaged stress tensor for a granular medium. European Journal of Mechanics-A/Solids, **22**(4): 567–582.
- Huang, S. and Tao, J. 2020. Modeling clam-inspired burrowing in dry sand using cavity expansion theory and dem. Acta Geotechnica, 1–22. doi:10.1007/s11440-020-00918-8.
- Huang, S., Tang, Y., Bagheri, H., Li, D., Ardente, A., Aukes, D., Marvi, H., and Tao, J. 2020. Effects of friction anisotropy on upward burrowing behavior of soft robots in granular materials. Advanced Intelligent Systems, **2**(6): 1–16. doi:10.1002/aisy.201900183.
- Itasca Consulting Group, 2017. PFC 3D (Particle Flow Code in 3 Dimensions) Version 5.0 Documentation Minneapolis, MN, USA.
- Jiang, M.J., Yu, H.S., and Harris, D. 2006. Discrete element modelling of deep penetration in granular soils. International journal for numerical and analytical methods in geomechanics, **30**(4): 335–361. doi:10.1002/nag.473.
- Jardine, R.J., Zhu, B.T., Foray, P., and Yang, Z.X. 2013. Measurement of stresses around closed-ended displacement piles in sand. Géotechnique, **63**(1): 1–17. doi:10.1680/geot.9.P.137.
- Khosravi, A., Martinez, A., DeJong, J.T., and Wilson, D. 2018, September. Discrete element simulations of bio-inspired self-burrowing probes in sands of varying density.

- In Proceedings of the Biomediated and Bioinspired Geotechnical (B2G) Conference, Atlanta, GA, 12–13.
- Khosravi, A., Martinez, A., and DeJong, J.T. 2020. Discrete element model (DEM) simulations of cone penetration test (CPT) measurements and soil classification. Canadian Geotechnical Journal, **57**(9): 1369–1387. doi:10.1139/cgj-2019-0512.
- Kurth, J.A. and Kier, W.M. 2014. Scaling of the hydrostatic skeleton in the earthworm Lumbricus terrestris. Journal of Experimental Biology, 217(11): 1860–1867. doi:10.1242/jeb.098137.
- Kuei, K.C., DeJong, J.T., and Martinez, A. 2020, February. Particle Size Effects on the Strength and Fabric of Granular Media. In Geo-Congress 2020: Modeling, Geomaterials, and Site Characterization, 349–358. Reston, VA: American Society of Civil Engineers.
- Lade, P.V., and Duncan, J.M. 1975. Elastoplastic stress-strain theory for cohesionless soil. Journal of Geotechnical and Geoenvironmental Engineering, 101(ASCE# 11670 Proceeding).
- Lin, J., and Wu, W. 2012. Numerical study of miniature penetrometer in granular material by discrete element method. Philosophical Magazine, 92(28-30): 3474–3482. doi:10.1080/14786435.2012.706373.
- Mayne, P.W. 2007. Cone penetration testing, 368. Transportation Research Board.
- Ma, Y., Evans, T.M., and Cortes, D.D. 2020. 2D DEM analysis of the interactions between bioinspired geo-probe and soil during inflation-deflation cycles. Granular Matter, 22(1): 1– 14. doi:10.1007/s10035-019-0974-7.
- Mair, R.J., and Wood, D.M. 1987. Pressuremeter testing: methods and interpretation. CIRIA Ground Engineering Report, London, UK.
- Mallett, S., Matsumura, S., and Frost, J.D. 2018. Additive manufacturing and computed tomography of bio-inspired anchorage systems. Geotechnique Letters, **8**(3): 1–7. doi:10.1680/jgele.18.00090.

- Martinez, A., and Frost, J.D. 2017. The influence of surface roughness form on the strength of sand-structure interfaces. Geotechnique Letters, **7**(1): 104-111. doi.org/10.1680/jgele.16.00169
- Martinez, A., Palumbo, S., and Todd, B.D. 2019. Bio-Inspiration for anisotropic load transfer at soil structure interfaces. Journal of Geotechnical and Geoenvironmental Engineering, **145**(10). doi:10.1061/(ASCE)GT.1943-5606.0002138.
- Martinez, A., DeJong, J.T., Jaeger, R.A., and Khosravi, A. 2020. Evaluation of self-penetration potential of a bio-inspired site characterization probe by cavity expansion analysis. Canadian Geotechnical Journal, **57**(5): 706–716. doi:10.1139/cgj-2018-0864.
- Martinez, A., DeJong, J., Akin, I., Aleali, A., Arson, C., Atkinson, J., Bandini, P., Baser, T.,
 Borela, R., Boulanger, R., Burrall, M., Chen, Y., Collins, C., Cortes, D., Dai, S., DeJong, T., Del Dottore, E., Dorgan, K., Fragaszy, R., Frost, D., Full, R., Ghayoomi, M.,
 Goldman, D., Gravish, N., Guzman, I.L., Hambleton, J., Hawkes, E., Helms, M., Hu,
 D.L., Huang, L., Huang, S., Hunt, C., Irschick, D., Lin, H., Lingwall, B., Marr, W.A.,
 Mazzolai, B., McInroe, B., Murthy, T., O'Hara, K., Porter, M., Sadek, S., Sanchez, M.,
 Santamarina, C., Shao, L., Sharp, J., Stuart, H., Stutz, H.H., Summers, A.P., Tao, J.,
 Tolley, M., Treers, L., Turnbull, K., Valdes, R., van Passen, L., Viggiani, G., Wilson, D.,
 Wu, W., Yu, X. and Zheng, J. Bio-inspired geotechnical engineering: principles, current work, opportunities and challenges. Geotechnique, 1-19. doi:10.1680/jgeot.20.P.170
- McDowell, G.R., Falagush, O., and Yu, H.S. 2012. A particle refinement method for simulating DEM of cone penetration testing in granular materials. Geotechnique Letters, **2**(3): 141–147. doi:10.1680/geolett.12.00036.
- Murphy, E.A., and Dorgan, K.M. 2011. Burrow extension with a proboscis: mechanics of burrowing by the glycerid Hemipodus simplex. Journal of Experimental Biology, **214**(6): 1017–1027. doi:10.1242/jeb.051227.

- Naclerio, N.D., Hubicki, C.M., Aydin, Y.O., Goldman, D.I., and Hawkes, E.W. 2018, October. Soft robotic burrowing device with tip-extension and granular fluidization. In 2018 IEEE/RSJ International Conference on Intelligent Robots and Systems (IROS), 5918–5923. IEEE. doi:10.1109/IROS.2018.8593530.
- O'Hara, K.B., and Martinez, A. 2020. Monotonic and cyclic frictional 1037 resistance directionality in snakeskin-inspired surfaces and piles. Journal of Geotechnical and Geoenvironmental Engineering, **146**(11). doi:10.1061/(ASCE)GT.1943-5606.0002368.
- Ortiz, D., Gravish, N., and Tolley, M.T. 2019. Soft robot actuation strategies for locomotion in granular substrates. IEEE Robotics and Automation Letters, **4**(3): 2630–2636. doi:10.1109/LRA.2019.2911844.
- O'Sullivan, C. 2011. Particulate discrete element modelling: a geomechanics perspective. CRC Press. doi:10.11475/sabo.67.5_77.
- Potyondy, D. 2009. Stiffness Matrix at a Contact Between Two Clumps Itasca Consulting Group, Inc., Minneapolis, MN, Technical Memorandum ICG6863-L.
- Purdy, C., Raymond, A.J., DeJong, J.T., and Kendall, A. 2020, February. Life Cycle Assessment of Site Characterization Methods. In Geo-Congress 2020: Geo-Systems, Sustainability, Geoenvironmental Engineering, and Unsaturated Soil Mechanics, 80–89. Reston, VA: American Society of Civil Engineers.
- Raymond, A.J., Tipton, J.R., Kendall, A., and DeJong, J.T. 2020. Review of impact categories and environmental indicators for life cycle assessment of geotechnical systems. Journal of Industrial Ecology, **24**(3): 485–499. doi:10.1111/jiec.12946.
- Radjai, F., and Richefeu, V. 2009. Contact dynamics as a nonsmooth discrete element method. Mechanics of Materials, **41**(6): 715–728. doi:10.1016/j.mechmat.2009.01.028.
- Robertson, P.K. 2016. Cone penetration test (CPT)-based soil behaviour type (SBT) classification system—an update. Canadian Geotechnical Journal, **53**(12): 1910–1927. doi: 10.1139/cgj-2016-0044.

- Ruiz, S., Or, D., and Schymanski, S.J. 2015. Soil penetration by earthworms and plant roots—mechanical energetics of bioturbation of compacted soils. PloS one, **10**(6), p.e0128914. doi:10.1371/journal.pone.0128914.
- Sadava, D.E., Hillis, D.M., Heller, H.C., and Berenbaum, M. 2009. Life: the science of biology (Vol. 2). Macmillan.
- Savioli, A., Viggiani, C., and Santamarina, J.C. 2014. Root-soil mechanical interaction. In Geo-Congress 2014: Geo-characterization and Modeling for Sustainability, 3977–3984. doi:10.1061/9780784413272.386.
- Sadeghi, A., Tonazzini, A., Popova, L., and Mazzolai, B. 2014. A novel growing device inspired by plant root soil penetration behaviors. PloS one, **9**(2), p.e90139. doi:10.1371/journal.pone.0090139.
- Salgado, R., and Prezzi, M. 2007. Computation of cavity expansion pressure and penetration resistance in sands. International Journal of Geomechanics, **7**(4): 251–265. doi:10.1061/(ASCE)1532-3641(2007)7:4(251).
- Sheng, D., Eigenbrod, K.D., and Wriggers, P. 2005. Finite element analysis of pile installation using large-slip frictional contact. Computers and Geotechnics, **32**(1): 17–26. doi:10.1016/j.compgeo.2004.10.004.
- Shi, W.C., Zhu, J.G., Chiu, C.F., and Liu, H.L. 2010. Strength and deformation behaviour of coarse-grained soil by true triaxial tests. Journal of Central South University of Technology, **17**(5): 1095–1102. doi:10.1007/s11771-010-0602-5.
- Shin, H., and Santamarina, J.C. 2011. Open-mode discontinuities in soils. Géotechnique Letters, **1**(4): 95–99. doi:10.1680/geolett.11.00014.
- Simoni A., and Houlsby G.T. 2006. The direct shear strength and dilatancy of sand-gravel mixtures. Geotechnical Geological Engineering, **24**(3):523–549. doi: 10.1007/s10706-004-5832-6.

- Stutz, H.H., and Martinez, A. 2021. Directionally-dependent strength and dilatancy behavior of soil-structure interfaces. Acta Geotechnica (published online). https://doi.org/10.1007/s11440-021-01199-5
- Tao, J., Huang, S., and Tang, Y. 2020. SBOR: a minimalistic soft self-burrowing-out robot inspired by razor clams. Bioinspiration and Biomimetics, 15(5), 1–22. doi:10.1088/1748-3190/ab8754.
- Trueman, E.R. 1968. A comparative account of the burrowing process of species of Mactra and of other bivalves. Journal of Molluscan Studies, **38**(2): 139–151. doi:10.1093/oxfordjournals.mollus.a065032.
- Trueman, E.R. 1968. Burrowing habit and the early evolution of body cavities. Nature, **218**(5136): 96–98. doi:10.1038/218096a0.
- Trueman, E.R. 1968. The locomotion of the freshwater clam Margaritifera margaritifera (Unionacea: Margaritanidae). Malacologia, **6**: 401–410.
- Wensrich, C.M., and Katterfeld, A. 2012. Rolling friction as a technique for modelling particle shape in DEM. Powder Technology, **217**: 409–417. doi:10.1016/j.powtec.2011.10.057.
- Xiao, Y., Sun, Y., Liu, H., and Yin, F. 2016. Critical state behaviors of a coarse granular soil under generalized stress conditions. Granular Matter, **18**(2), p.17. doi: 10.1007/s10035-016-0623-3.
- Yang, J., and Luo, X.D. 2018. The critical state friction angle of granular materials: does it depend on grading?." Acta Geotechnica, 13(3): 535-547. doi: 10.1007/s11440-017-0581-x.
- Yu, H.S., and Houlsby, G.T. 1991. Finite cavity expansion in dilatant soils: loading analysis. Geotechnique, **41**(2): 173–183. doi:10.1680/geot.1991.41.2.173.
- Yu, H.S., Schnaid, F., and Collins, I.F. 1996. Analysis of cone pressuremeter tests in sands. Journal of Geotechnical Engineering, 122(8):623-632. doi:10.1061/(ASCE)0733-9410(1996)122:8(623).

- Zeng, Z., and Chen, Y. 2016. Simulation of soil-micropenetrometer interaction using the discrete element method (DEM). Transactions of the ASABE, **59**(5): 1157–1163. doi:10.13031/trans.59.11726.
- Zhang, Z., and Wang, Y.H. 2015. Three-dimensional DEM simulations of monotonic jacking in sand. Granular Matter, **17**(3): 359–376. doi:10.1007/s10035-015-0562-4.
- Zhang, N., Arroyo, M., Ciantia, M.O., Gens, A., and Butlanska, J. 2019. Standard penetration testing in a virtual calibration chamber. Computers and Geotechnics, 111: 277–289. doi:10.1016/j.compgeo.2019.03.021.

Table 1. DEM Simulation Parameters.

Input Parameter	Symbol	Value
Normal Stiffness to Particle Diameter	k_n/d	1.0E+08
Normal to Shear Stiffness Ratio	k_n/k_s	1.5
Sliding Friction Coefficient	μ	0.4
Rolling Friction Coefficient	μ_{rr}	0.4
Ball-probe Friction Coefficient	μ_p	0.3
Ball-wall Friction Coefficient	μ'	0.1
Particle Density (kg/m³)	G_{s}	2650
Local Damping of Sample Preparation	ξ	0.6

Table 2. DEM Simulation Matrix.

#	Parameter	Name	Anchor Length, L	Anchor-Tip Distance, H
1	Reference	H4L4	4 D _{probe}	4 D _{probe}
2	Н	H1L4	4 D _{probe}	1 D _{probe}
3	L	H4L8	8 D _{probe}	4 D _{probe}
4	Danastahilita	H4L4-R1	4 D	4 D
5	Repeatability	H4L4-R2	4 D _{probe}	4 D _{probe}

CP stage AE stage TA stage # Name $P_b(kPa)$ q_c (MPa) q_c (MPa) P_a(kPa) q_c (MPa) $P_a(kPa)$ H4L4 4.80 753 4.50 957 3.36 362 704 312 676 H4L4-R1 4.74 3.53 4.33 H4L4-R2 4.76 776 3.84 4.16 346 900

Table 3. Summary of repeated reference simulations.

FIGURE LIST

Figure 1. Soil penetration in geotechnical applications, polychaete burrowing and plant root growth, and open-mode discontinuity. (a) in-situ cone penetration test uses the weight of drill rigs as reaction for probe penetration, (b) pile driving uses impact loading applied by a hammer, (c) polychaete in photoelastic gel showing zones with stress concentration and relaxation (after Dorgan 2007), (d) results of finite element simulation of plant growth showing stress relaxation in warmer colors (after Savioli et al. 2014), and (e) results of numerical study on open-mode discontinuity showing stress relaxation ahead of the invasive immiscible phase (after Shin and Santamarina 2010).

Figure 2. DEM simulations model: (a) calibration chamber and simulated probe; (b) configuration of measurement spheres (note: purple spheres are used to plot stress paths of soils around the anchor and tip).

Figure 3. Results of triaxial compression tests and cone penetration tests at confining pressures of 5, 25, 100, and 400 kPa. Evolution with axial strain of (a) deviatoric stress and (b) volumetric strain and stress paths in (c) q-p' plane and (d) e-p' plane; signatures of (e) tip penetration resistance and (f) soil behavior type classification based on penetration resistance measurements. **Figure 4.** (a) Probe configuration parameters and (b) schematic of the three simulation stages. The arrows acting against the probe represent soil stresses or forces acting on it (Notes: each simulation includes the three stages (CP, AE, TA), the motion of the tip and anchor during TA is

controlled using the algorithm described in Figure 5, and during TA the shaft located above the anchor remains stationary).

Figure 5. Logic for velocity-controlled motion with force limits for the tip and the anchor during Tip Advancement (TA) stage (note: F represents either of the total force F_t or Q_t ; ΔF is 50 N and less than 1% F_t or Q_t).

Figure 6. Time histories of DEM simulation. Stresses and displacements of the probes with (a) H=4Dprobe, L=4Dprobe (H4L4), (b) H=1Dprobe, L=4Dprobe (H1L4), and (c) H=4Dprobe, L=8Dprobe (H4L8) (note: \overline{N} is normalized timestep, CP occurs when $\overline{N} \in [0,1]$, AE occurs when $\overline{N} \in [1,2]$, TA occurs when $\overline{N} \in [2,3]$).

Figure 7. Time histories of total reaction and resistance forces and displacements of the probes with (a) H=4Dprobe, L=4Dprobe (H4L4), (b) H=1Dprobe, L=4Dprobe (H1L4), and (c) H=4Dprobe, L=8Dprobe (H4L8) during Tip Advancement (TA) (note: \overline{N} is normalized timestep, CP occurs when $\overline{N} \in [0,1]$, AE occurs when $\overline{N} \in [1,2]$, TA occurs when $\overline{N} \in [2,3]$).

Figure 8. (a) Force chain maps and (b) stress state maps at the end of Cone Penetration stage.

Figure 9. Maps of (a) mean (b) radial and (c) vertical effective stresses at the end of the cone penetration (CP) stage ($\overline{N} = 1$) and maps of (d) volumetric, (e) radial and (f) vertical strains for the last 0.1 m of CP (note: dilatant volumetric strains and compressive strain components are defined as positive).

Figure 10. Stress paths in q-p' plane and e-p' plane and evolution of b values during the last 0.1 m of the Cone Penetration (CP) stage for soil (a–c) near the tip and (d–f) near the anchors. **Figure 11.** (a–c) Soil force chains and (d–f) stress state maps for simulations at the end of Anchor Expansion stage ($\overline{N} = 2$).

Figure 12. Change in (a–c) soil major principal stresses, (d–f) radial stresses, and (g–i) vertical stresses maps at the end of the Anchor Expansion stage ($\overline{N} = 2$).

- **Figure 13.** (a–c) Soil volumetric, (d–f) radial strain, and (g–i) vertical strain maps for simulations during Anchor Expansion stage (note: dilatant volumetric strains and compressive strain components are defined as positive).
- **Figure 14.** Stress paths in q-p' plane and e-p' plane and evolution of b values during the Anchor Expansion (AE) stage for soil (a–c) near the tip and (d–f) near the anchors.
- **Figure 15.** (a–c) Soil force chain and (a–c) stress state maps for simulations at the end of the Tip Advancement stage ($\overline{N} = 3$).
- **Figure 16.** Change in (a–c) soil major principal stresses, (d–f) radial stresses, and (g–i) vertical stresses at the end of the Tip Advancement stage ($\overline{N} = 3$).
- **Figure 17.** (a–c) Soil volumetric strains, (d–f) radial strains, and (g–i) vertical strains strain maps for simulations during the Tip Advancement stage (note: dilatant volumetric strains and compressive strain components are defined as positive).
- **Figure 18.** Stress paths in q-p' plane and e-p' plane and evolution of b values during the Tip Advancement stage for soil (a–c) near the tip and (d–f) near the anchors.
- **Figure S1.** (a) Distribution of ring radius along chamber height during the Cone Penetration stage and (b) ring stresses at the end of the Cone Penetration stage (note: Ring 1 and Ring 14 are not in contact with particles, therefore they are not shown in (b)).

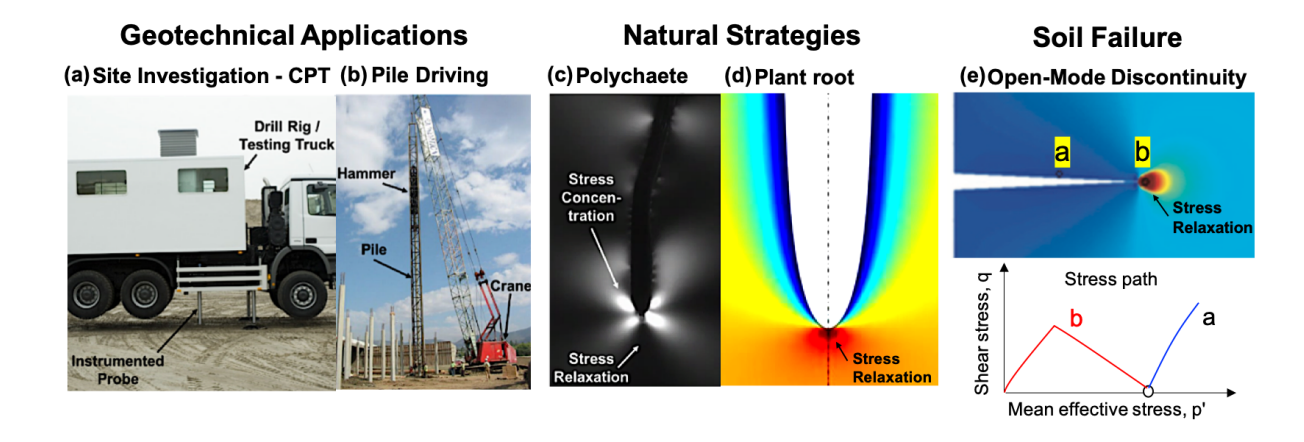


Figure 1. Soil penetration in geotechnical applications, polychaete burrowing and plant root growth, and open-mode discontinuity. (a) in-situ cone penetration test uses the weight of drill rigs as reaction for probe penetration, (b) pile driving uses impact loading applied by a hammer, (c) polychaete in photoelastic gel showing zones with stress concentration and relaxation (after Dorgan 2007), (d) results of finite element simulation of plant growth showing stress relaxation in warmer colors (after Savioli et al. 2014), and (e) results of numerical study on open-mode discontinuity showing stress relaxation ahead of the invasive immiscible phase (after Shin and Santamarina 2010).

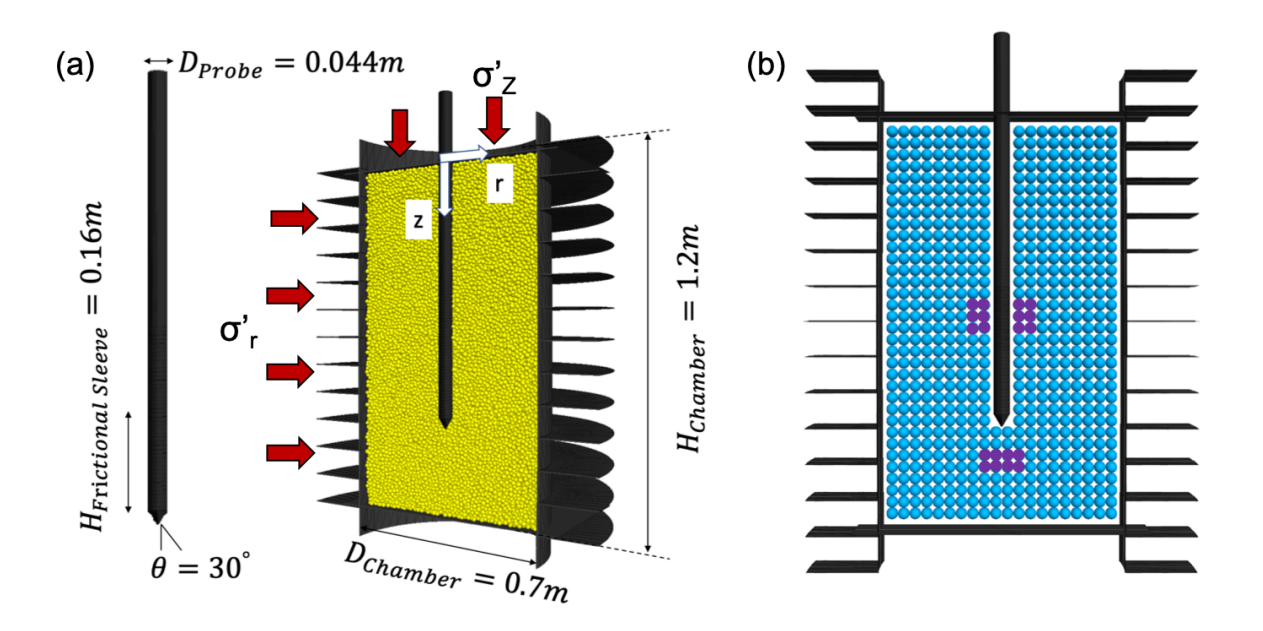


Figure 2. DEM simulations model: (a) calibration chamber and simulated probe; (b) configuration of measurement spheres (note: purple spheres are used to plot stress paths of soils around the anchor and tip).

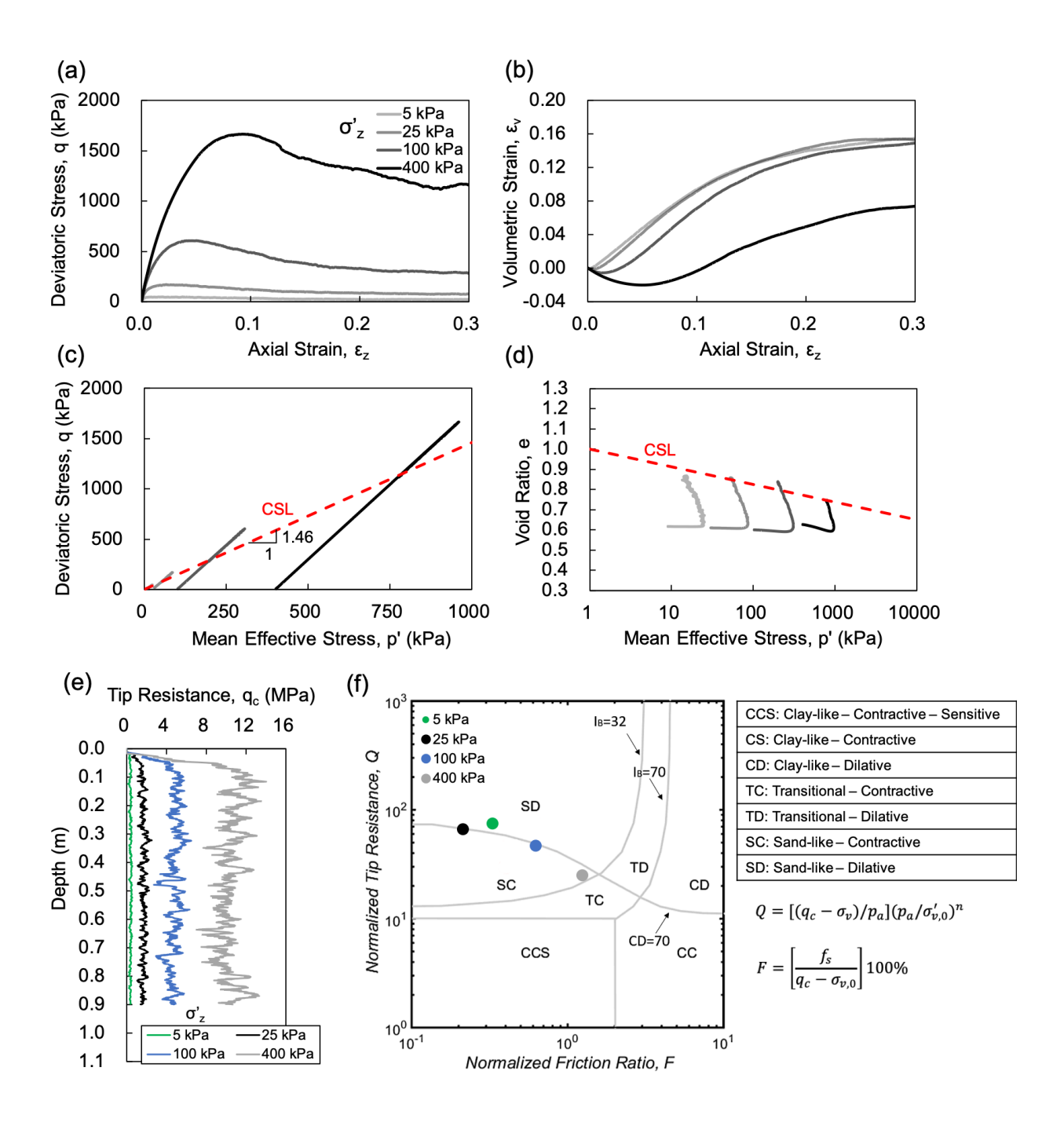


Figure 3. Results of triaxial compression tests and cone penetration tests at confining pressures of 5, 25, 100, and 400 kPa. Evolution with axial strain of (a) deviatoric stress and (b) volumetric strain and stress paths in (c) q-p' plane and (d) e-p' plane; signatures of (e) tip penetration resistance and (f) soil behavior type classification based on penetration resistance measurements.

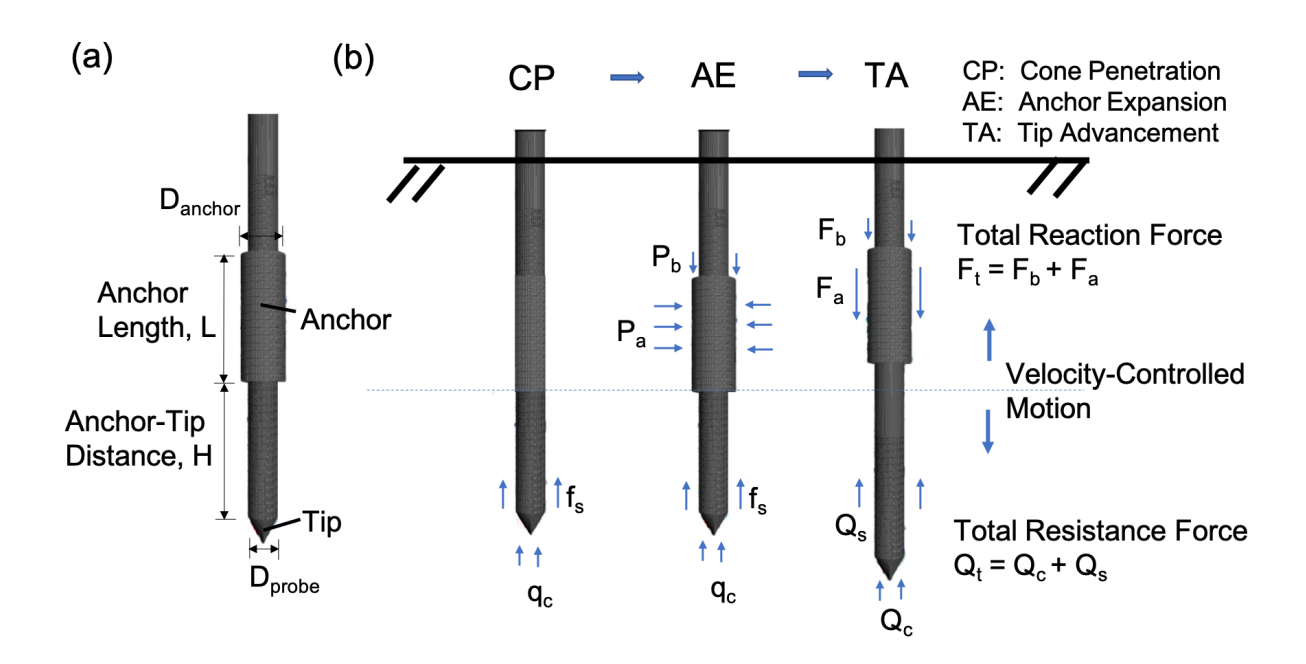


Figure 4. (a) Probe configuration parameters and (b) schematic of the three simulation stages. The arrows acting against the probe represent soil stresses or forces acting on it (Notes: each simulation includes the three stages (CP, AE, TA), the motion of the tip and anchor during TA is controlled using the algorithm described in Figure 5, and during TA the shaft located above the anchor remains stationary).

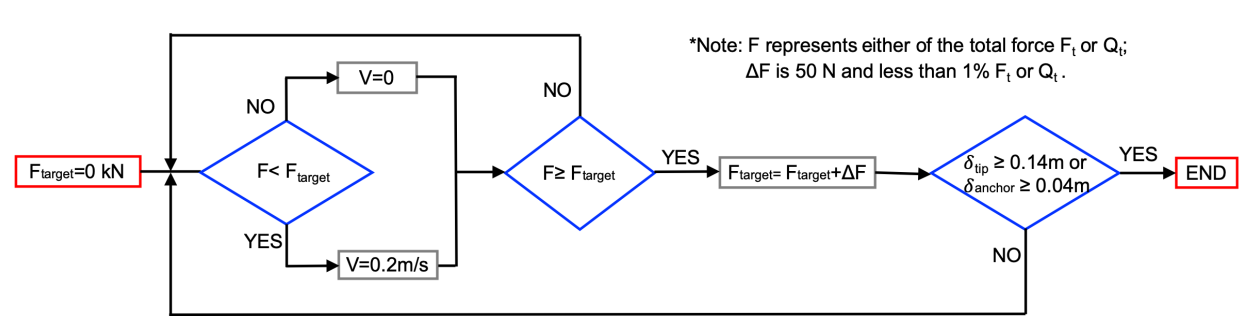


Figure 5. Logic for velocity-controlled motion with force limits for the tip and the anchor during Tip Advancement (TA) stage (note: F represents either of the total force F_t or Q_t ; ΔF is 50 N and less than 1% F_t or Q_t).

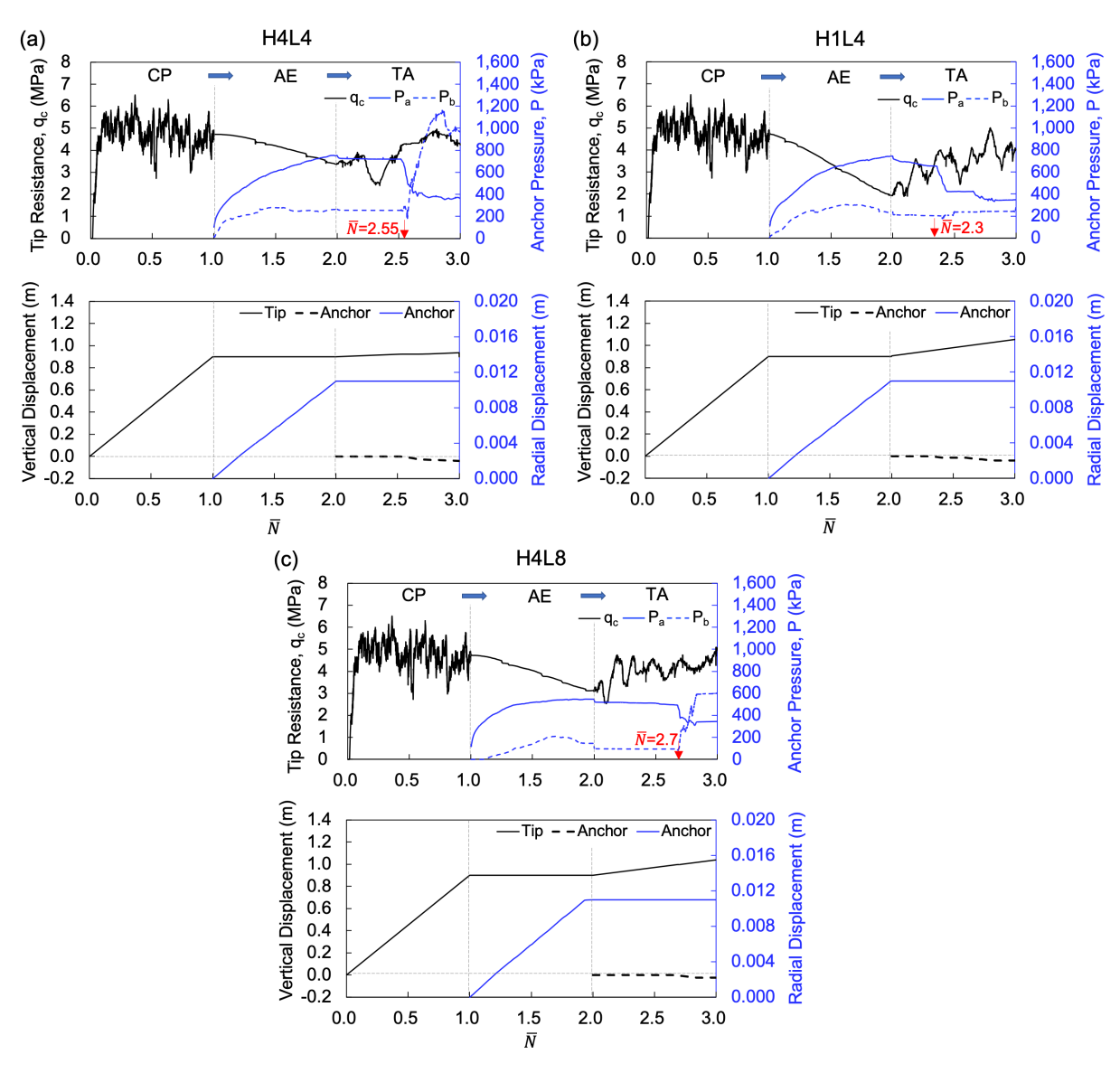


Figure 6. Time histories of DEM simulation. Stresses and displacements of the probes with (a) H=4D_{probe}, L=4D_{probe} (H4L4), (b) H=1D_{probe}, L=4D_{probe} (H1L4), and (c) H=4D_{probe}, L=8D_{probe} (H4L8) (note: \overline{N} is normalized timestep, CP occurs when $\overline{N} \in [0,1]$, AE occurs when $\overline{N} \in [1,2]$, TA occurs when $\overline{N} \in [2,3]$).

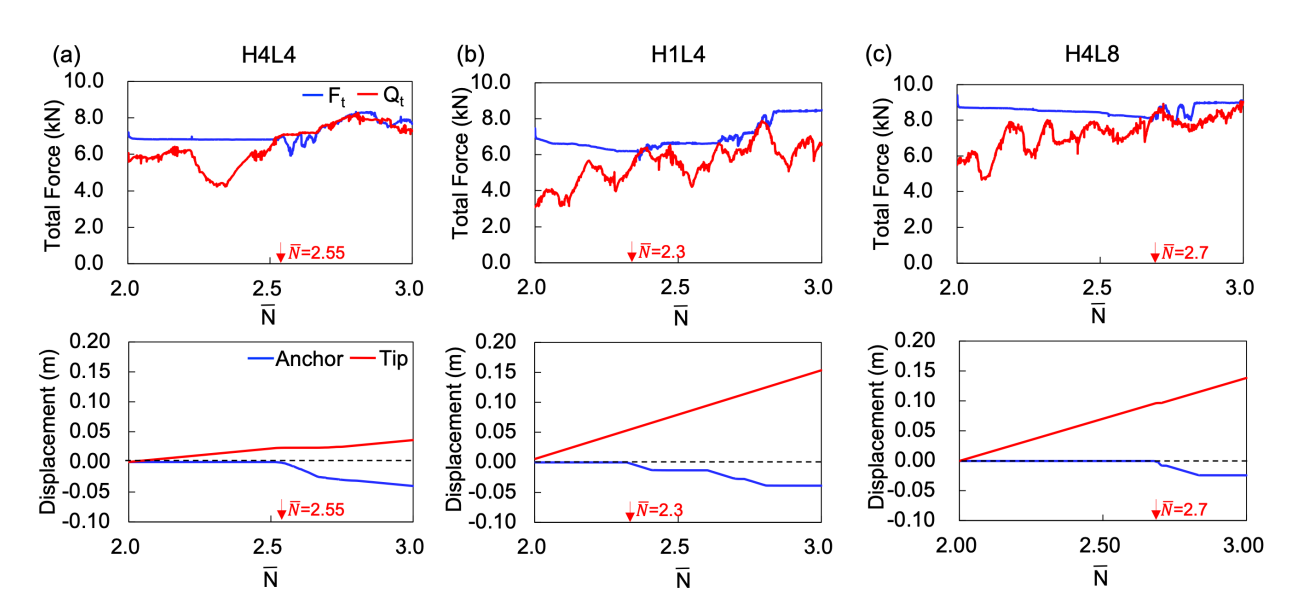


Figure 7. Time histories of total reaction and resistance forces and displacements of the probes with (a) H=4D_{probe}, L=4D_{probe} (H4L4), (b) H=1D_{probe}, L=4D_{probe} (H1L4), and (c) H=4D_{probe}, L=8D_{probe} (H4L8) during Tip Advancement (TA) (note: \overline{N} is normalized timestep, CP occurs when $\overline{N} \in [0,1]$, AE occurs when $\overline{N} \in [1,2]$, TA occurs when $\overline{N} \in [2,3]$).

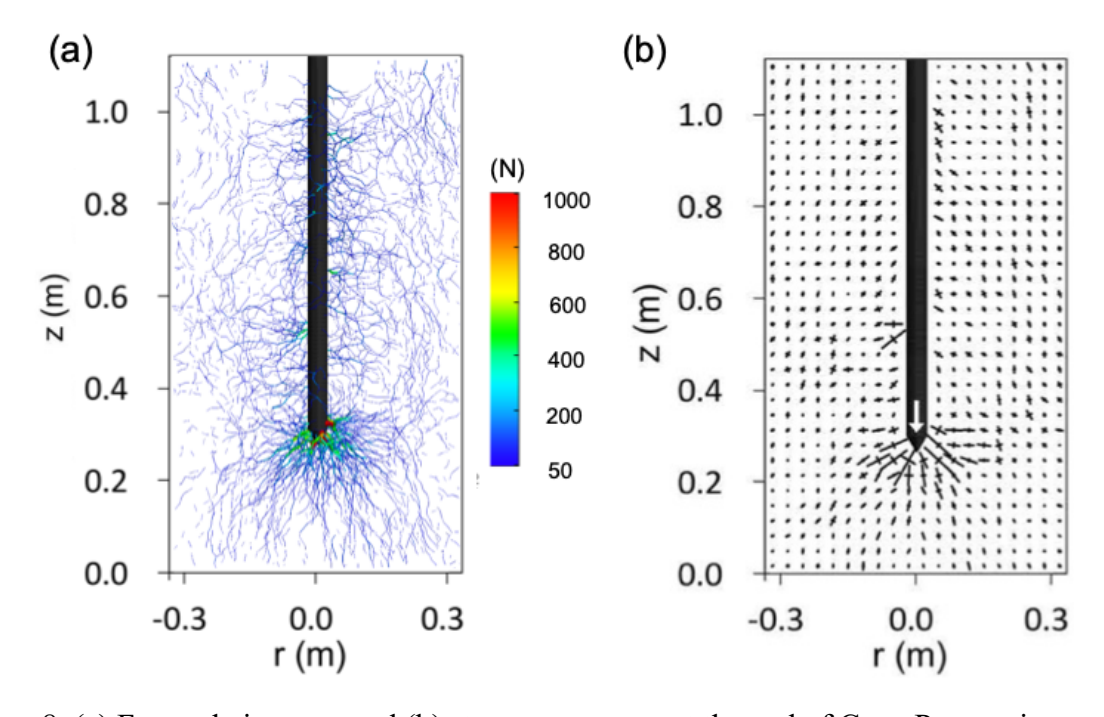


Figure 8. (a) Force chain maps and (b) stress state maps at the end of Cone Penetration stage.

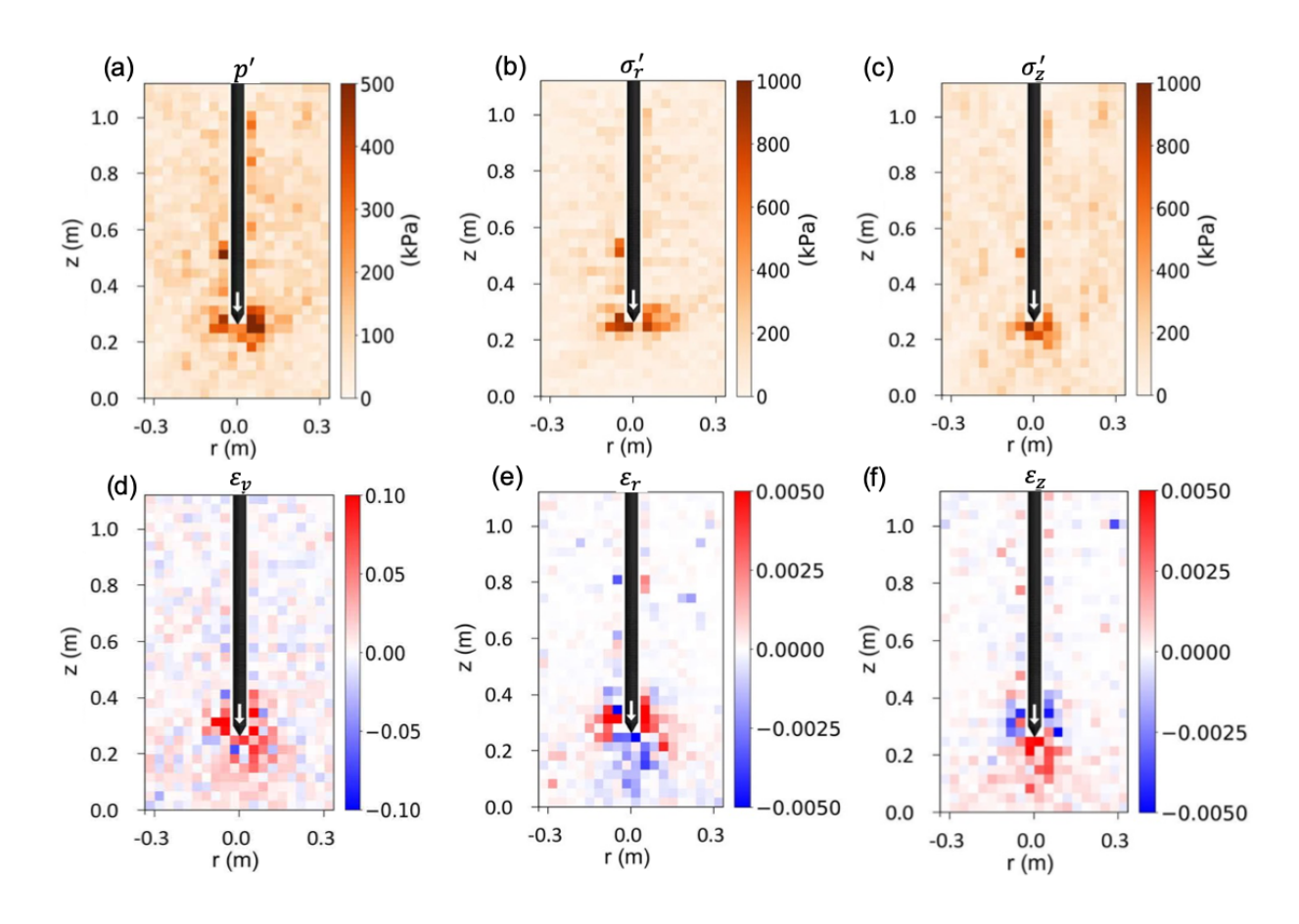


Figure 9. Maps of (a) mean (b) radial and (c) vertical effective stresses at the end of the cone penetration (CP) stage ($\overline{N} = 1$) and maps of (d) volumetric, (e) radial and (f) vertical strains for the last 0.1 m of CP (note: dilatant volumetric strains and compressive strain components are defined as positive).

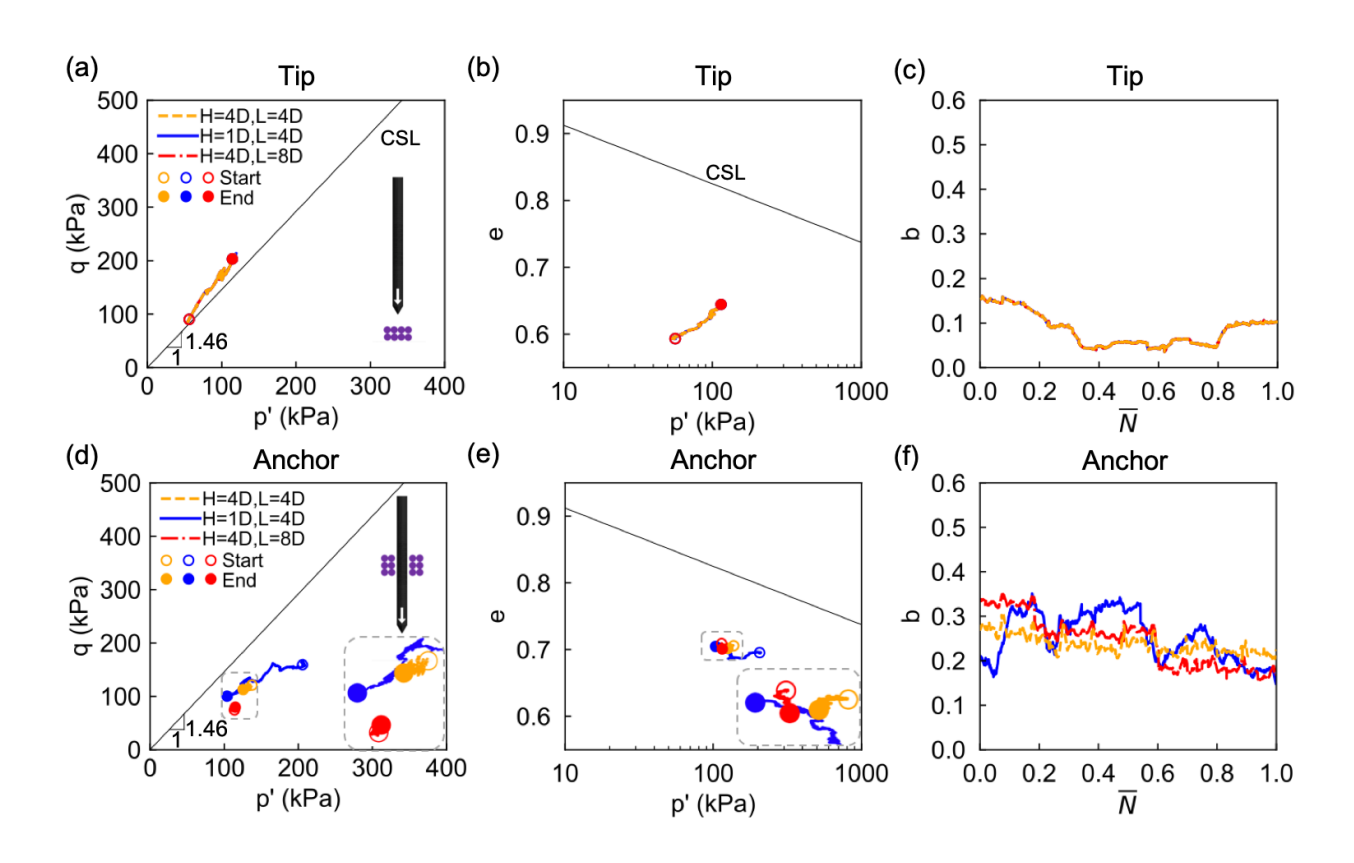


Figure 10. Stress paths in q-p' plane and e-p' plane and evolution of b values during the last 0.1 m of the Cone Penetration (CP) stage for soil (a-c) near the tip and (d-f) near the anchors.

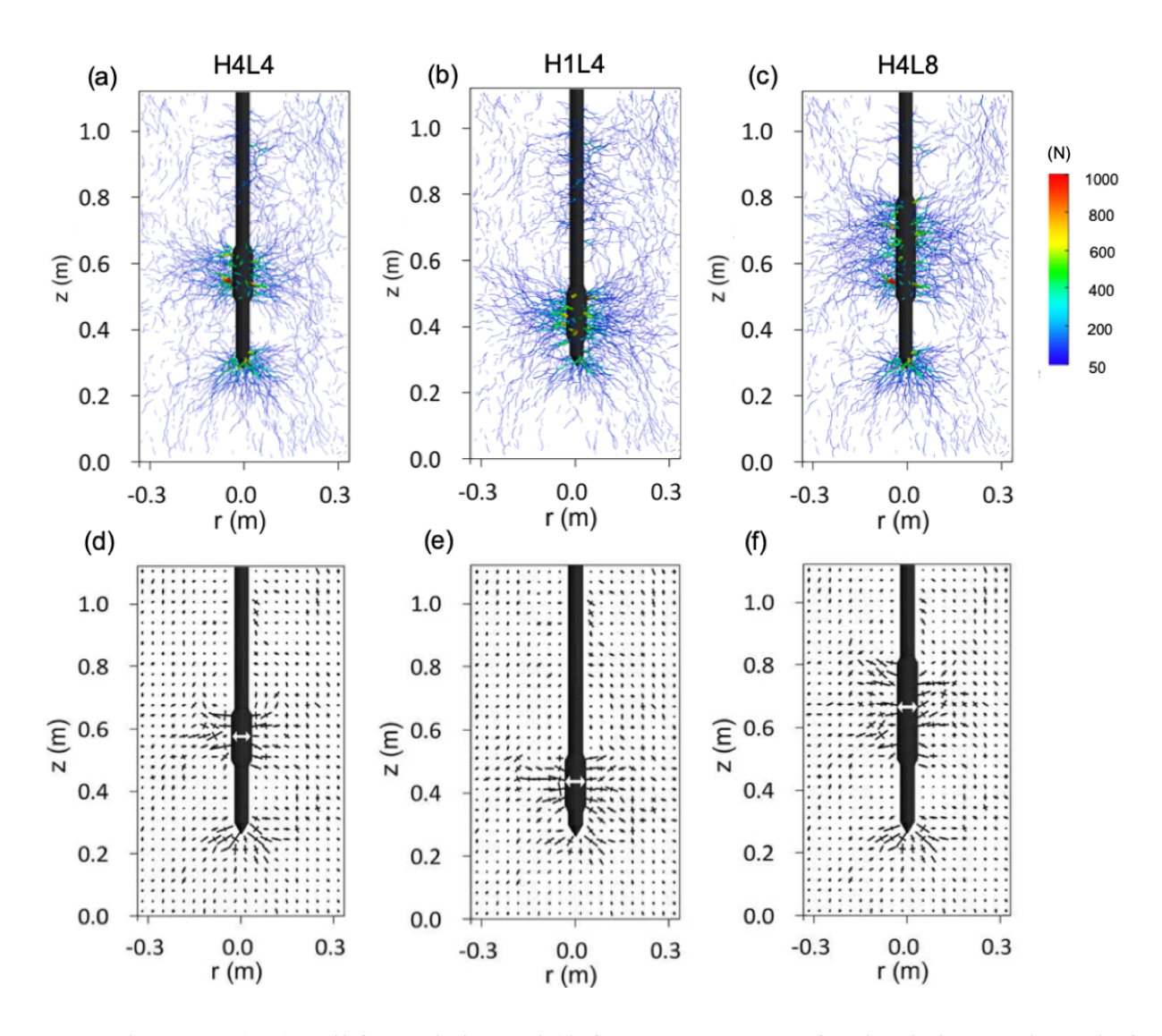


Figure 11. (a–c) Soil force chains and (d–f) stress state maps for simulations at the end of Anchor Expansion stage ($\overline{N} = 2$).

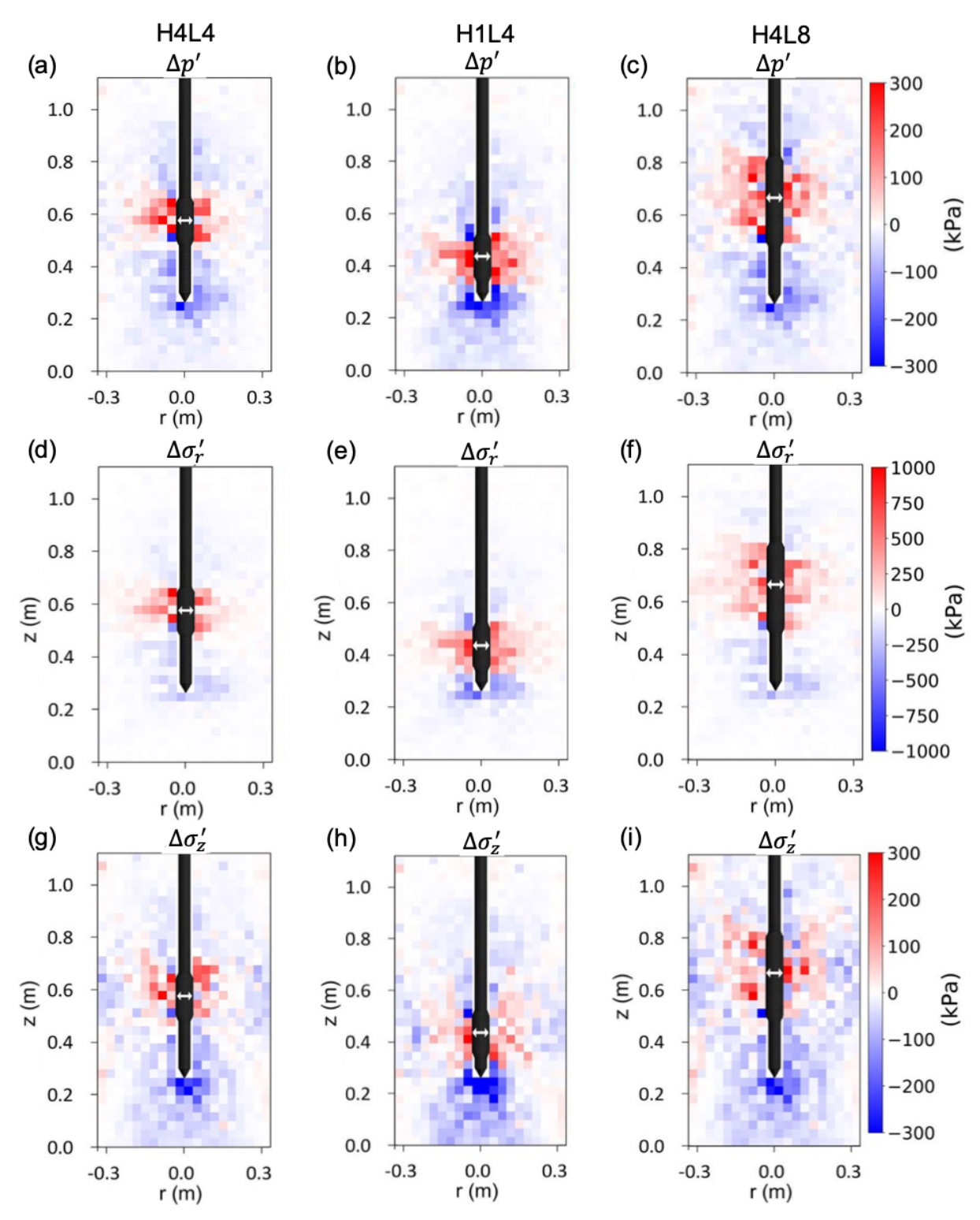


Figure 12. Change in (a–c) soil major principal stresses, (d–f) radial stresses, and (g–i) vertical stresses maps at the end of the Anchor Expansion stage ($\overline{N} = 2$).

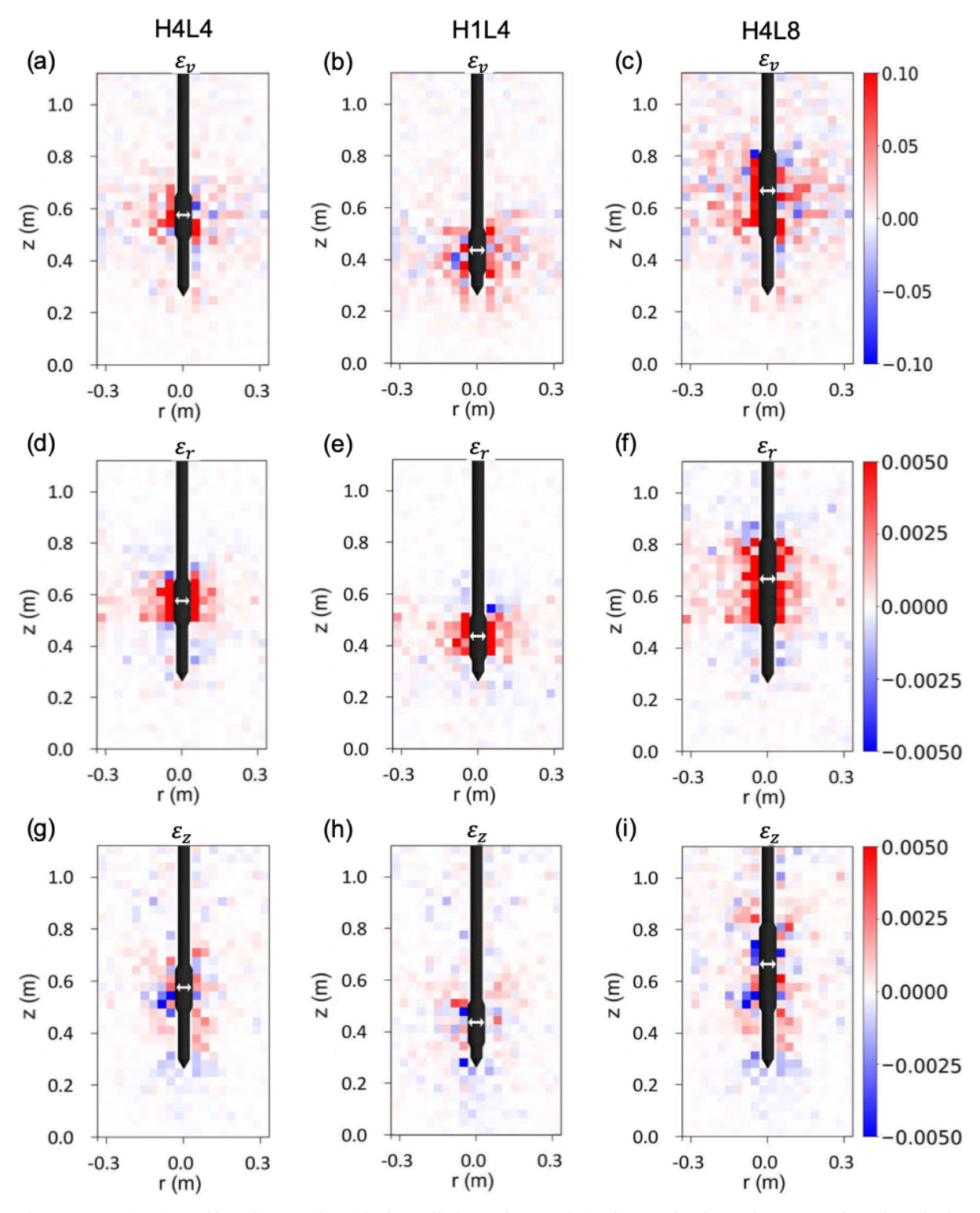


Figure 13. (a–c) Soil volumetric, (d–f) radial strain, and (g–i) vertical strain maps for simulations during Anchor Expansion stage (note: dilatant volumetric strains and compressive strain components are defined as positive).

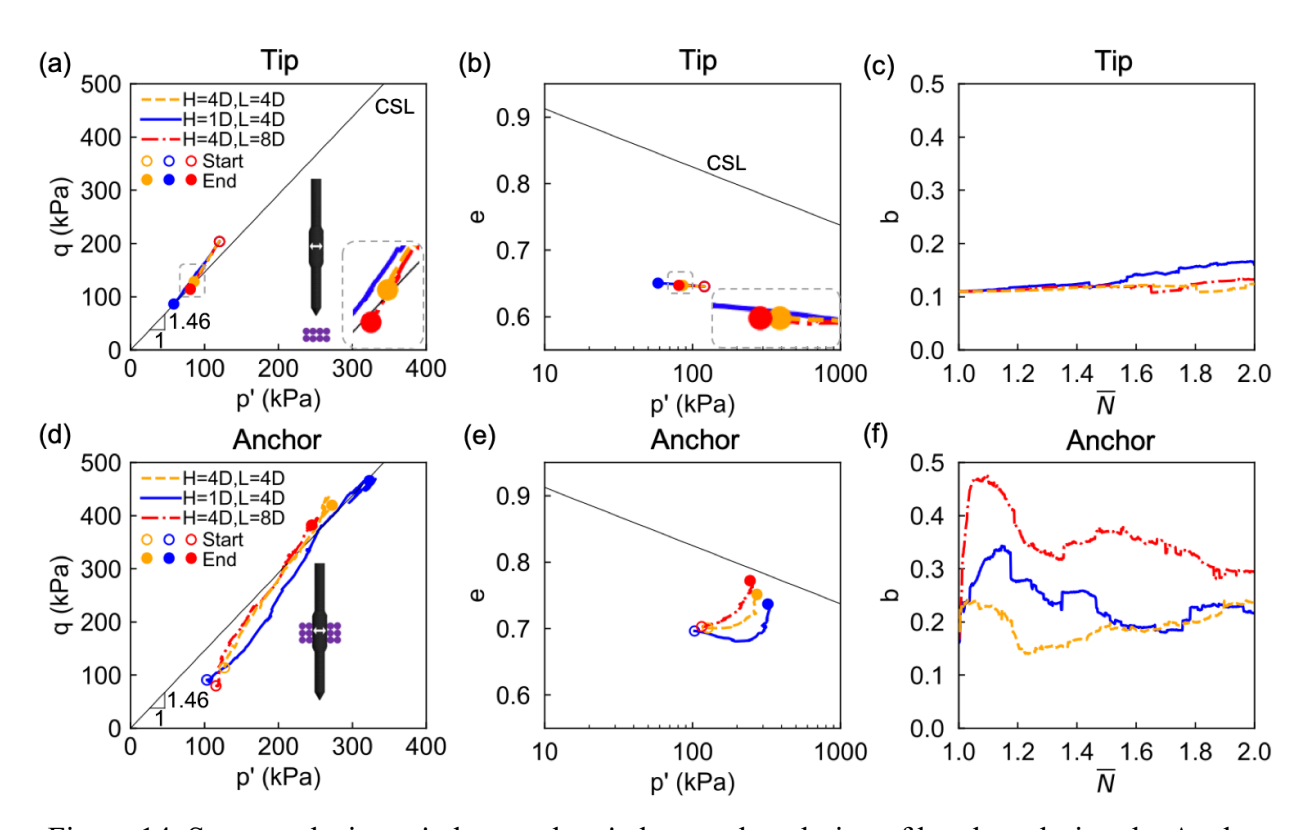


Figure 14. Stress paths in q-p' plane and e-p' plane and evolution of b values during the Anchor Expansion (AE) stage for soil (a-c) near the tip and (d-f) near the anchors.

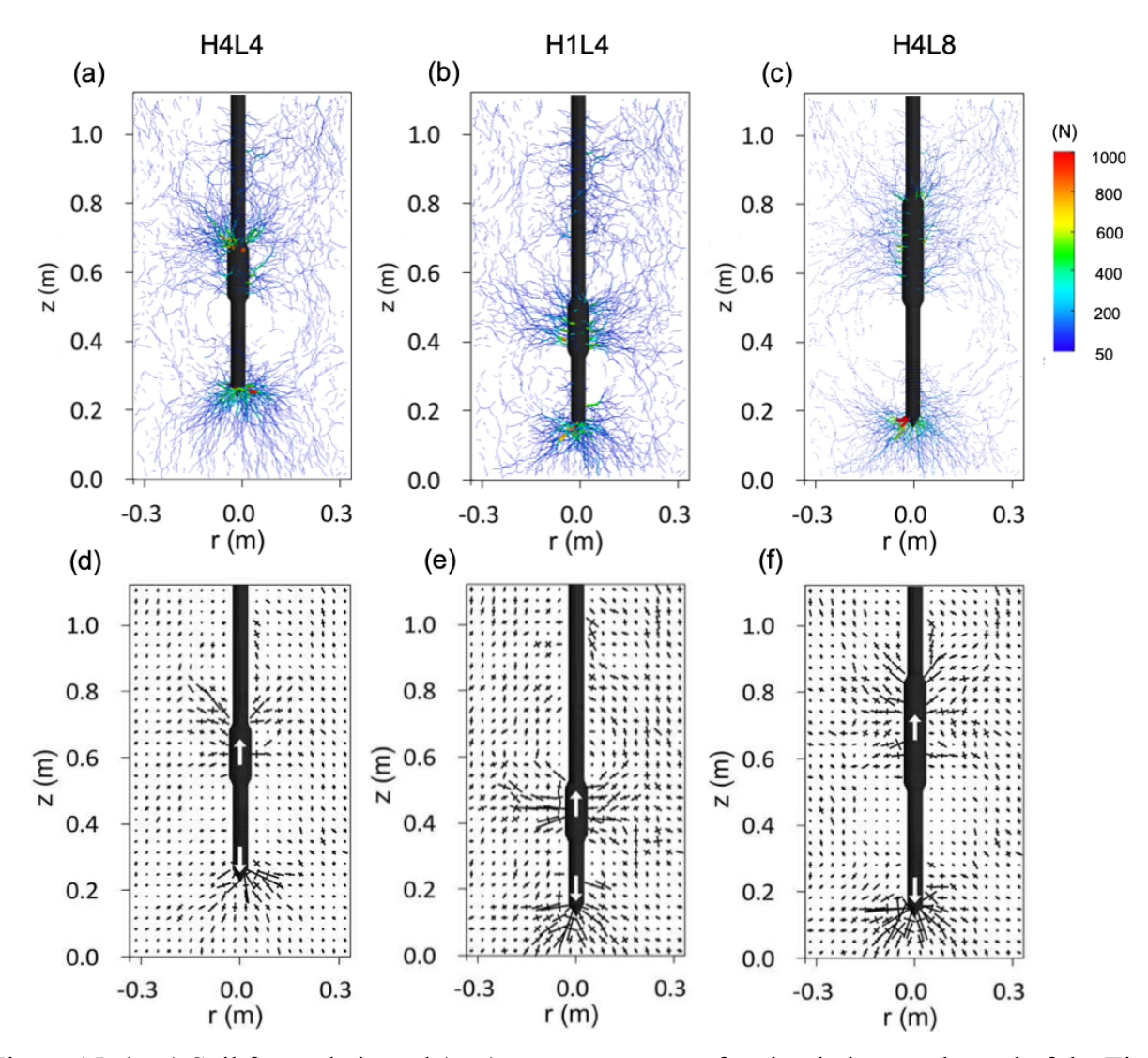


Figure 15. (a–c) Soil force chain and (a–c) stress state maps for simulations at the end of the Tip Advancement stage ($\overline{N} = 3$).

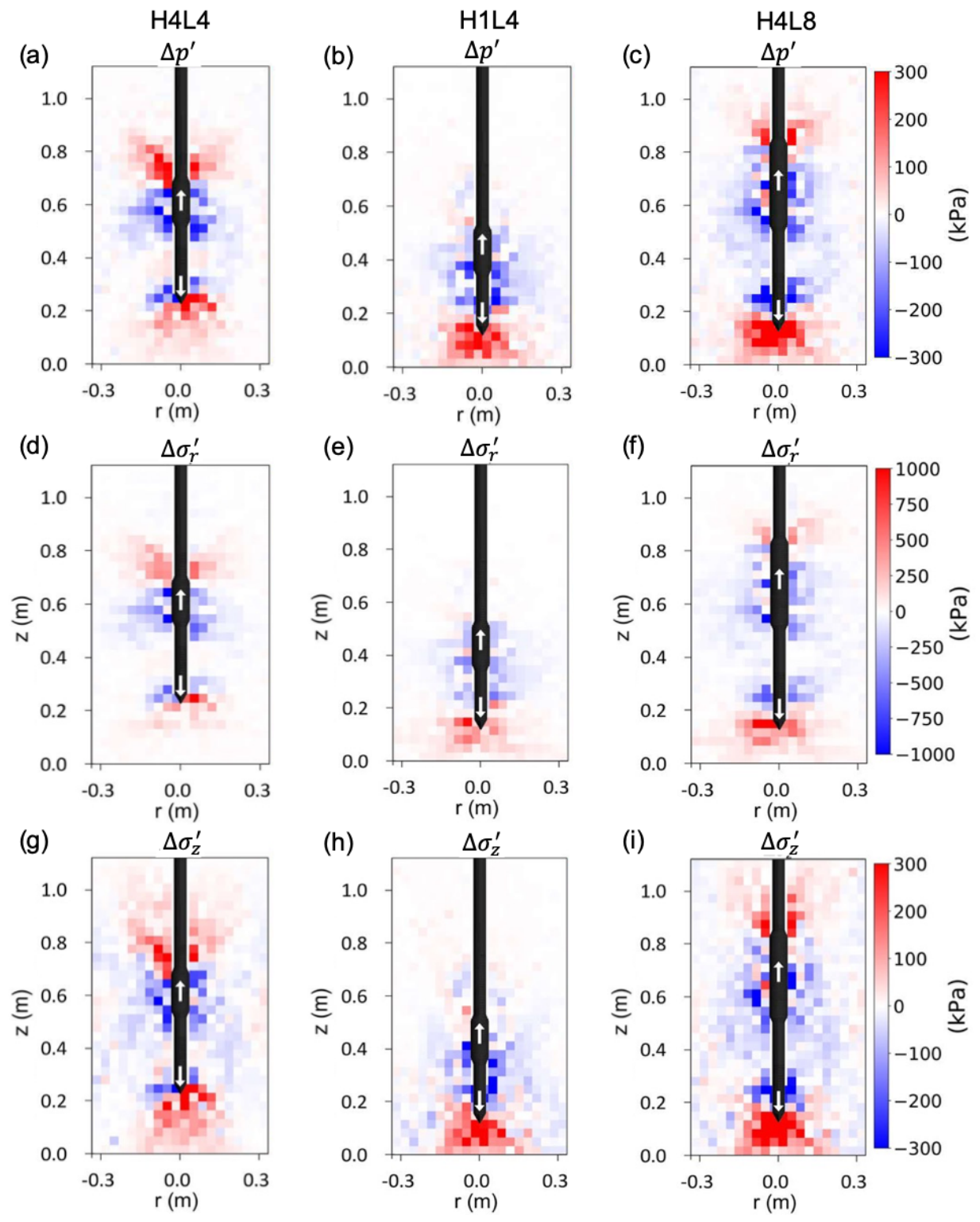


Figure 16. Change in (a–c) soil major principal stresses, (d–f) radial stresses, and (g–i) vertical stresses at the end of the Tip Advancement stage ($\overline{N} = 3$).

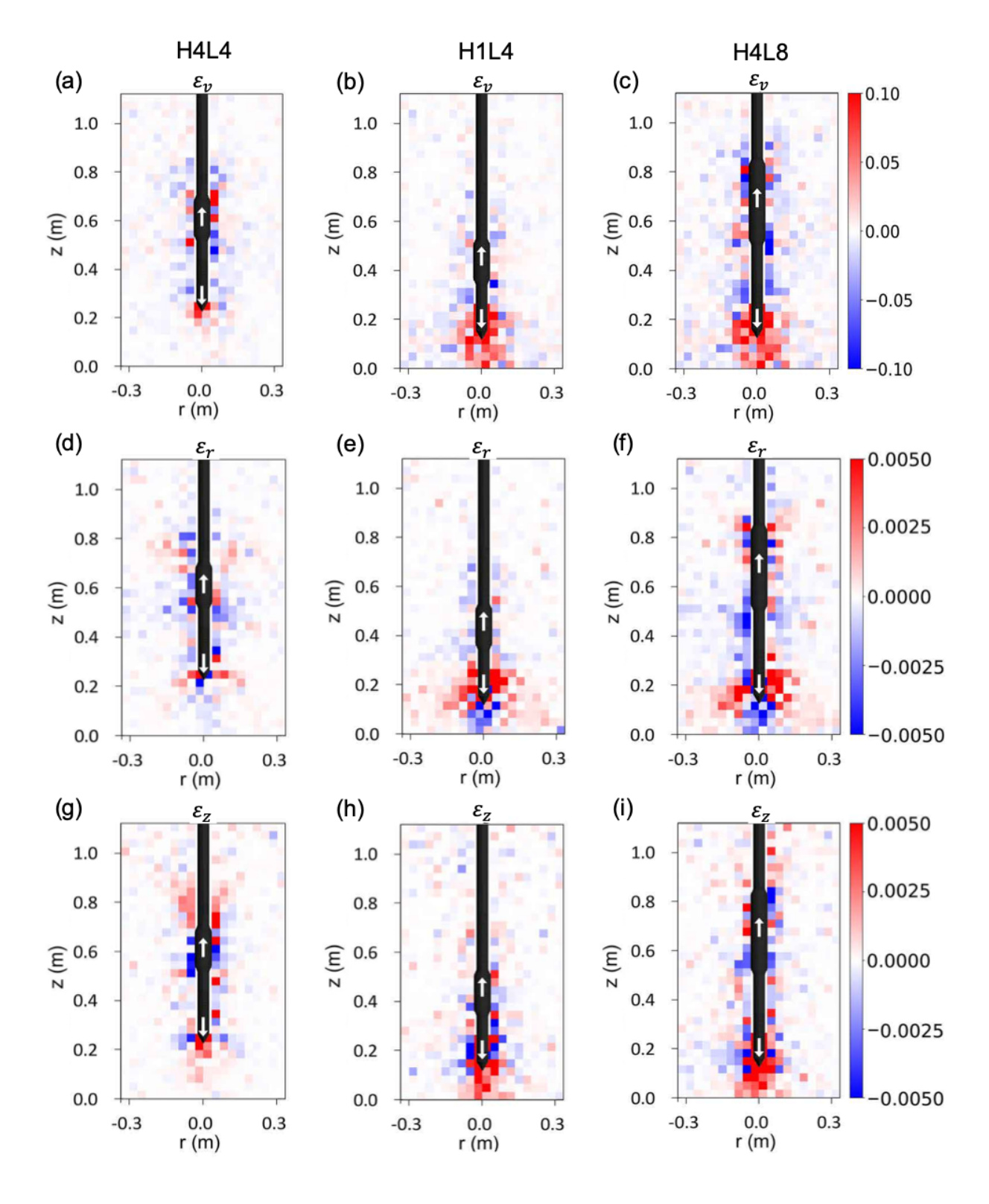


Figure 17. (a–c) Soil volumetric strains, (d–f) radial strains, and (g–i) vertical strains strain maps for simulations during the Tip Advancement stage (note: dilatant volumetric strains and compressive strain components are defined as positive).

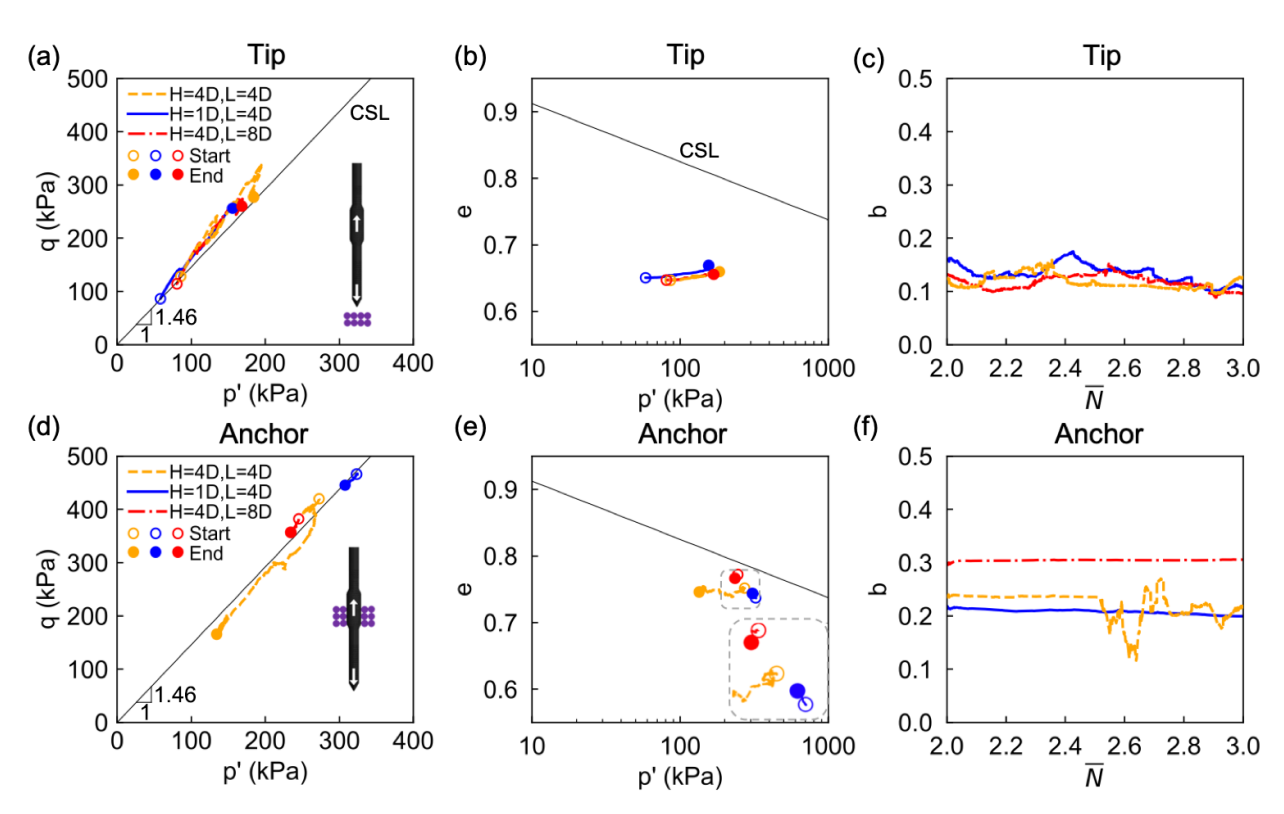


Figure 18. Stress paths in q-p' plane and e-p' plane and evolution of b values during the Tip Advancement stage for soil (a–c) near the tip and (d–f) near the anchors.

SUPPLEMENTARY FIGURES

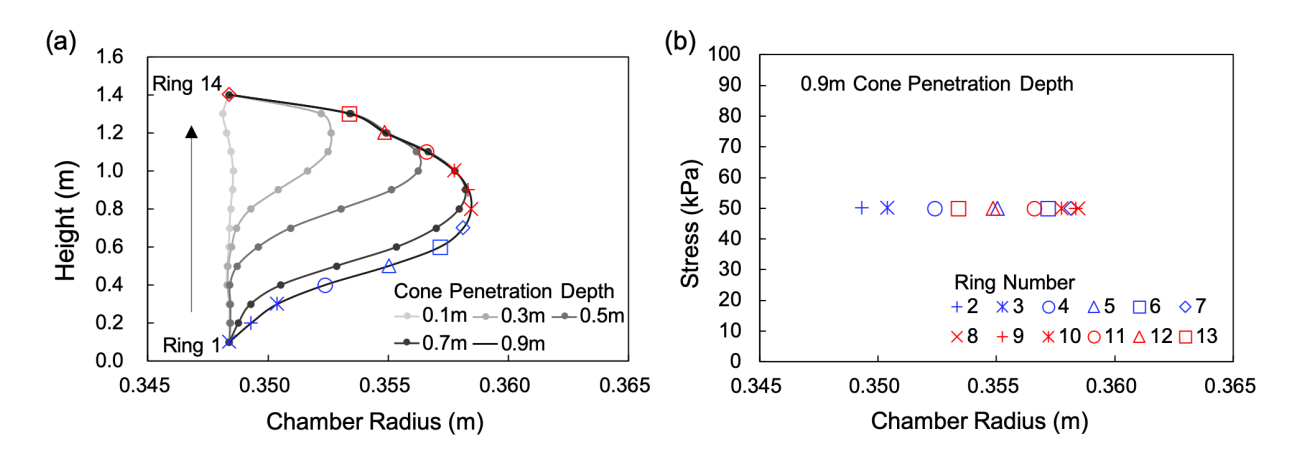


Figure S1. (a) Distribution of ring radius along chamber height during the Cone Penetration stage and (b) ring stresses at the end of the Cone Penetration stage (note: Ring 1 and Ring 14 are not in contact with particles, therefore they are not shown in (b)).